A&A 578, A105 (2015)
DOI: 10.1051/0004-6361/201322786


Astronomy & Astrophysics

# Extreme emission-line galaxies out to $z \sim 1$ in zCOSMOS

## I. Sample and characterization of global properties⋆

R. Amorín[1,2], E. Pérez-Montero[2,3,4], T. Contini[3,4], J. M. Vílchez[2], M. Bolzonella[10], L. A. M. Tasca[6], F. Lamareille[3,4], G. Zamorani[10], C. Maier[5,16], C. M. Carollo[5], J.-P. Kneib[6], O. Le Fèvre[6], S. Lilly[5], V. Mainieri[7], A. Renzini[8], M. Scodeggio[9], S. Bardelli[10], A. Bongiorno[11], K. Caputi[21], O. Cucciati[13], S. de la Torre[12], L. de Ravel[12], P. Franzetti[9], B. Garilli[9,6], A. Iovino[14], P. Kampczyk[5], C. Knobel[5], K. Kovač[5,15], J.-F. Le Borgne[3,4], V. Le Brun[6], M. Mignoli[10], R. Pellò[3,4], Y. Peng[5], V. Presotto[17,14], E. Ricciardelli[18], J. D. Silverman[19], M. Tanaka[19], L. Tresse[6], D. Vergani[10,20], and E. Zucca[10]

[1] INAF–Osservatorio Astronomico di Roma, via Frascati 33, 00040 Monteporzio Catone, Roma, Italy
e-mail: ricardo.amorin@oa-roma.inaf.it
[2] Instituto de Astrofísica de Andalucía, CSIC, 18008 Granada, Spain
[3] IRAP, Université de Toulouse, UPS-OMP, Toulouse, France
[4] Institut de Recherche en Astrophysique et Planétologie, CNRS, 14 avenue Édouard Belin, 31400 Toulouse, France
[5] Institute of Astronomy, ETH Zurich, 8093 Zürich, Switzerland
[6] Laboratoire d'Astrophysique de Marseille, CNRS-Université d'Aix-Marseille, 38 rue Frederic Joliot Curie, 13388 Marseille, France
[7] European Southern Observatory, Karl-Schwarzschild-Strasse 2, 85748 Garching b. Muenchen, Germany
[8] Dipartimento di Astronomia, Universitá di Padova, vicolo Osservatorio 3, 35122 Padova, Italy
[9] INAF–IASF Milano, via Bassini 15, 20133 Milano, Italy
[10] INAF–Osservatorio Astronomico di Bologna, via Ranzani 1, 40127 Bologna, Italy
[11] Max-Planck-Institut für extraterrestrische Physik, 85748 Garching b. Muenchen, Germany
[12] SUPA Institute for Astronomy, The University of Edinburgh, Royal Observatory, Edinburgh, EH9 3HJ, UK
[13] INAF–Osservatorio Astronomico di Trieste, via Tiepolo, 11, 34143 Trieste, Italy
[14] INAF–Osservatorio Astronomico di Brera, via Brera, 28, 20159 Milano, Italy
[15] MPA – Max-Planck Institut für Astrophysik, Karl-Schwarzschild-Str. 1, 85741 Garching, Germany
[16] University of Vienna, Department of Astronomy, Tuerkenschanzstrasse 17, 1180 Vienna, Austria
[17] Universitá degli Studi dell'Insubria, via Valleggio 11, 22100 Como, Italy
[18] Instituto de Astrofísica de Canarias, vía Lactea s/n, 38200 La Laguna, Tenerife, Spain
[19] IPMU, Institute for the Physics and Mathematics of the Universe, 5-1-5 Kashiwanoha, 277-8583 Kashiwa, Japan
[20] INAF–IASFBO, via P. Gobetti 101, 40129 Bologna, Italy
[21] Kapteyn Astronomical Institute, University of Groningen, 9700 AV Groningen, The Netherlands

Received 3 October 2013 / Accepted 16 March 2015

**ABSTRACT**

*Context.* The study of large and representative samples of low-metallicity star-forming galaxies at different cosmic epochs is of great interest to the detailed understanding of the assembly history and evolution of low-mass galaxies.
*Aims.* We present a thorough characterization of a large sample of 183 extreme emission-line galaxies (EELGs) at redshift $0.11 \leq z \leq 0.93$ selected from the 20k zCOSMOS bright survey because of their unusually large emission line equivalent widths.
*Methods.* We use multiwavelength COSMOS photometry, HST-ACS $I$-band imaging, and optical zCOSMOS spectroscopy to derive the main global properties of star-forming EELGs, such as sizes, stellar masses, star formation rates (SFR), and reliable oxygen abundances using both "direct" and "strong-line" methods.
*Results.* The EELGs are extremely compact ($r_{50} \sim 1.3$ kpc), low-mass ($M_* \sim 10^7$–$10^{10}\,M_\odot$) galaxies forming stars at unusually high specific star formation rates ($sSFR \equiv SFR/M_\star$ up to $10^{-7}$ yr$^{-1}$) compared to main sequence star-forming galaxies of the same stellar mass and redshift. At rest-frame UV wavelengths, the EELGs are luminous and show high surface brightness and include strong Ly$\alpha$ emitters, as revealed by GALEX spectroscopy. We show that zCOSMOS EELGs are high-ionization, low-metallicity systems, with median $12+\log(\mathrm{O/H}) = 8.16 \pm 0.21$ ($0.2\,Z_\odot$) including a handful of extremely metal-deficient ($<0.1\,Z_\odot$) EELGs. While ~80% of the EELGs show non-axisymmetric morphologies, including clumpy and cometary or tadpole galaxies, we find that ~29% of them show additional low-surface-brightness features, which strongly suggests recent or ongoing interactions. As star-forming dwarfs in the local Universe, EELGs are most often found in relative isolation. While only very few EELGs belong to compact groups, almost one third of them are found in spectroscopically confirmed loose pairs or triplets.
*Conclusions.* The zCOSMOS EELGs are galaxies caught in a transient and probably early period of their evolution, where they are efficiently building up a significant fraction of their present-day stellar mass in an ongoing, galaxy-wide starburst. Therefore, the EELGs constitute an ideal benchmark for comparison studies between low- and high-redshift low-mass star-forming galaxies.

**Key words.** galaxies: evolution – galaxies: fundamental parameters – galaxies: abundances – galaxies: starburst – galaxies: irregular – galaxies: star formation

⋆ Full Tables 1 and 2 are only available at the CDS via anonymous ftp to cdsarc.u-strasbg.fr (130.79.128.5) or via http://cdsarc.u-strasbg.fr/viz-bin/qcat?J/A+A/578/A105

## 1. Introduction

Low-mass galaxies undergoing vigorous bursts of star formation over galaxy-wide scales provide unique laboratories for understanding galaxy mass assembly and chemical evolution over cosmic times. In the local Universe, these systems are often referred to as HII galaxies (Terlevich et al. 1991) and blue compact dwarfs (BCDs; Thuan & Martin 1981), depending on the observational technique or the selection criteria (see Kunth & Östlin 2000, for a review). In spectroscopic surveys, they are generally recognized by their high-excitation emission lines with unusually large equivalent widths (EW)[1], as a product of the photoionization of gas by hot massive stars in a young burst of star formation (Sargent & Searle 1970).

Over the last decade, the advent of all-sky optical and UV surveys such as the Sloan Digital Sky Survey (SDSS; Abazajian et al. 2003) and the Galaxy Evolution Explorer (GALEX; Martin et al. 2005), along with other smaller surveys, have allowed us to systematically search and characterize relatively large samples of extreme emission-line galaxies (EELGs) out to the frontiers of the local Universe ($z \lesssim 0.3$, e.g., Kniazev et al. 2004; Kakazu et al. 2007; Overzier et al. 2008; Salzer et al. 2009; Cardamone et al. 2009; Cowie et al. 2010; Izotov et al. 2011; Shim & Chary 2013). This has made it possible to discover an increasing number of extremely compact, low-metallicity galaxies with unusually high specific star formation rates (SFR, s$SFR$ = $SFR/M_\star \sim 1{-}100\,\mathrm{Gyr}^{-1}$), such as the green peas (Cardamone et al. 2009; Amorín et al. 2010) and a handful of extremely metal-poor galaxies (XMPs; $Z \lesssim 0.1\,Z_\odot$ Kunth & Östlin 2000) at $0.1 \lesssim z \lesssim 0.4$ (e.g., Kakazu et al. 2007; Hu et al. 2009; Cowie et al. 2010).

Similarly to nearby HII galaxies and some BCDs, EELGs are probably the youngest and chemically least evolved population of low-$z$ star-forming galaxies (SFGs, e.g., Searle & Sargent 1972; Rosa-González et al. 2007; Jaskot & Oey 2013). These properties make them unique probes with which to study the details of chemical enrichment, massive star formation, and feedback processes in galaxies with physical properties (i.e., size, mass, SFR, metallicity, gas, and dust relative content) most closely resembling those prevailing at high redshift, e.g., Lyman-break galaxies and Lyman-$\alpha$ emitters (e.g., Pettini et al. 2001; Finkelstein et al. 2011). Furthermore, increasing observational evidence point to EELGs as the likely environments to host the progenitors of long-duration gamma-ray bursts (e.g., Christensen et al. 2004; Kewley et al. 2007; Savaglio et al. 2009; Guseva et al. 2011) and the most luminous supernovae (Chen et al. 2013; Lunnan et al. 2013; Leloudas et al. 2015; Thöne et al. 2014).

In order to understand comprehensively the properties of EELGs as a class, to select best case studies for detailed analysis, and to provide a valuable benchmark for comparative studies at higher redshifts, large and representative samples of EELGs must be assembled. Although EELGs are generally rare among local low-mass galaxies (<0.5% of galaxies in SDSS; Kniazev et al. 2004), their frequency and significance in the context of the cosmic star formation rate density is expected to increase out to $z \sim 1$ (Guzman et al. 1997; Kakazu et al. 2007). However, because of their faintness and compactness, studying EELGs at these intermediate redshifts requires a great deal of observational effort. Thus, pioneering studies have been limited to relatively small samples of intrinsically luminous objects (e.g., Koo et al. 1995; Phillips et al. 1997).

[1] We use the convention of positive equivalent widths for emission lines.

In this context, recent deep multiwavelength surveys have offered a new avenue for studying chemical enrichment and starburst activity and its associated feedback processes in strongly star-forming EELGs out to $z \sim 1$ and beyond (see, e.g., Hoyos et al. 2005; van der Wel et al. 2011; Atek et al. 2011; Trump et al. 2011; Xia et al. 2012; Henry et al. 2013; Ly et al. 2014; Amorín et al. 2014a,b; Masters et al. 2014; Maseda et al. 2014). This is the case of the COSMOS survey (Scoville et al. 2007) and one of its spectroscopic follow-ups, the zCOSMOS 20k bright survey (Lilly et al. 2007). In particular, the wealth of high-quality photometric and spectroscopic data provided by these surveys allow us to perform a thorough and systematic characterization of a large probe of faint ($I_{\mathrm{AB}} \lesssim 22.5$ mag) EELGs out to $z \sim 1$.

While the large collection of deep broad- and narrow-band photometric measurements provided by COSMOS allows luminosities and reliable stellar masses to be derived, HST-ACS $I$-band imaging provides the spatial resolution required to study morphological properties. Moreover, zCOSMOS provides the high signal-to-noise (S/N) spectroscopy required to properly measure the emission lines used to derive reliable gas-phase metallicities. Remarkably, and despite the challenge of measuring temperature sensitive emission line ratios (e.g., [O III] 5007/4363), zCOSMOS spectroscopy allows gas-phase metallicity to be derived using the so-called direct ($T_e$) an unprecedentedly large number of EELGs at intermediate redshifts. Thus, our survey offers the opportunity of identifying a relatively large number of extremely metal-deficient ($\lesssim 0.1\,Z_\odot$) galaxy candidates.

This is the first of a series of papers aimed at investigating the formation history and evolution of low-mass star-forming galaxies over cosmological time scales using deep multiwavelength surveys. Here, we present the largest spectroscopic sample of galaxies with extreme nebular emission in the range $0.1 \lesssim z \lesssim 1$ assembled so far. We characterize more than 150 EELGs selected from the zCOSMOS 20k bright survey, based on different key properties, namely size, stellar mass, metallicity, and SFR, which are discussed as a function of morphology and environment. The derived properties will be used in a companion paper (Amorín et al., in prep.; Paper II) to discuss possible evolutionary scenarios based on their position in scaling relations involving mass, size, metallicity, and SFR.

Our paper is organized as follows. In Sect. 2 we describe the parent sample, our dataset, and the selection criteria adopted to compile the sample of EELGs. In Sect. 3 we present the main physical properties of the sample. We describe the methodology used to derive stellar masses, star formation rates and UV properties, and gas-phase metallicities. As part of the analysis, we also present an alternative method aimed at obtaining $T_e$-based metallicities in those EELGs without available measurements of the [O II] 3727,3729 doublet. We finish Sect. 3 by studying the morphological and environmental properties of EELGs. Later, in Sects. 4–6, we highlight the discovery of a number of extremely metal-poor galaxy candidates, discuss the connection between EELGs and Ly$\alpha$ emitters, and compare the zCOSMOS EELGs with other previous samples. Finally, Sect. 7 summarizes our main results and conclusions.

Throughout this paper we adopt the standard $\Lambda$-CDM cosmology, i.e., $h = 0.7$, $\Omega_m = 0.3$, and $\Omega_\Lambda = 0.7$ (Spergel et al. 2007) and a solar metallicity value of $12+\log(\mathrm{O/H}) = 8.69$ (Allende Prieto et al. 2001). Magnitudes are given in the AB system.

## 2. Sample and data

### 2.1. The parent zCOSMOS 20k bright sample

COSMOS is a large HST-ACS survey, with $I$-band exposures down to $I_{AB} = 28$ on a field of 1.7 deg$^2$ (Scoville et al. 2007). The COSMOS field has been the object of extensive multiwavelength ground- and space-based observations spanning the entire spectrum: X-ray, UV, optical/NIR, mid-infrared, mm/submillimeter, and radio, providing photometry over 30 bands (Hasinger et al. 2007; Taniguchi et al. 2007; Capak et al. 2007; Lilly et al. 2007; Sanders et al. 2007; Bertoldi et al. 2007; Schinnerer et al. 2007; Koekemoer et al. 2007; McCracken et al. 2010).

The zCOSMOS survey (Lilly et al. 2007) is a large spectroscopic follow-up undertaken in the COSMOS field, which used about 600 h of ESO observing time with the VIMOS multi-object spectrograph (Le Fèvre et al. 2003) mounted on the Melipal 8 m telescope of the VLT. The survey was divided in two parts, zCOSMOS-bright and zCOSMOS-deep. The zCOSMOS-deep observed ~10 000 galaxies selected through color criteria to have $1.4 \lesssim z \lesssim 3.0$ on the central 1 deg$^2$ of the COSMOS field. The zCOSMOS-bright survey is purely magnitude-limited in $I$-band and covered the whole area of 1.7 deg$^2$ of the COSMOS field. The zCOSMOS-bright survey provides redshifts for ~20 000 galaxies down to $I_{AB} \leq 22.5$ as measured from the HST-ACS imaging. The success rate in redshift measurements is very high, 95% in the redshift range $0.5 < z < 0.8$, and the velocity accuracy is ~100 km s$^{-1}$ (Lilly et al. 2009). Each observed object has been assigned a flag according to the reliability of its measured redshift. Classes 3.x and 4.x redshifts, plus Classes 1.5, 2.4, 2.5, 9.3, and 9.5 are considered a secure set, with an overall reliability of 99% (see for details Lilly et al. 2009).

The current work is based on the zCOSMOS-bright survey final release, the 20k-bright sample. This catalog consists of about 20 000 spectra for galaxies with $z \leq 2$ and secure redshifts according to the above flag classification. The zCOSMOS-bright data were acquired with 1″ slits and the medium-resolution ($R = 600$) grism of VIMOS, providing spectra sampled at ~2.5 Å pixel$^{-1}$ over a wavelength range of approximately 5550–9650 Å. This spectral range enables important diagnostic emission lines to be followed in order to compute metallicity up to redshift $z \sim 1.5$. The observations were acquired with a seeing lower than 1.2″. The total integration time was set to 1 h to secure redshifts with a high success rate. Detailed information about target selection, observations, and data reduction can be found in Lilly et al. (2009).

Spectroscopic measurements (emission and absorption lines fluxes, and equivalent widths) in zCOSMOS were performed with the automated pipeline platefit-vimos (Lamareille et al., in prep.) similar to those performed on SDSS (e.g., Tremonti et al. 2004) and VVDS spectra (Lamareille et al. 2009). This routine fits the stellar component of galaxy spectra as a combination of 30 single stellar population (SSP) templates, with different ages and metallicities from the library of Bruzual & Charlot (2003). The best-fit synthetic spectrum is used to remove the stellar component. Emission lines are then fit as a single nebular spectrum made of a sum of Gaussians at specified wavelengths. Further details can be found in Lamareille et al. (2006a, 2009).

### 2.2. The EELG sample selection

In Pérez-Montero et al. (2013) we selected a large subsample of more than 5300 star-forming galaxies at redshift $z = 0-1.3$ from the 20k-bright sample to study their physical properties and chemical evolution. In order to define our sample of EELGs, we repeat the same procedure, discarding all broad-line AGNs and selecting only galaxies with $S/N > 2$ for all the emission-lines automatically measured by platefit-vimos, and involved in the derivation of the oxygen abundance. We limit the sample to ~5000 galaxies in the redshift range $0.11 \leq z \leq 0.93$ to keep only galaxies with [O III] $\lambda$5007 still included in the observed spectral range. Finally, from this subset we select ~200 galaxies with the largest rest-frame equivalent widths in [O III] $\lambda$5007, $EW$([O III]) ≥ 100 Å. The remaining galaxies – hereafter referred to as the SFG-20k sample – are used as a comparison set.

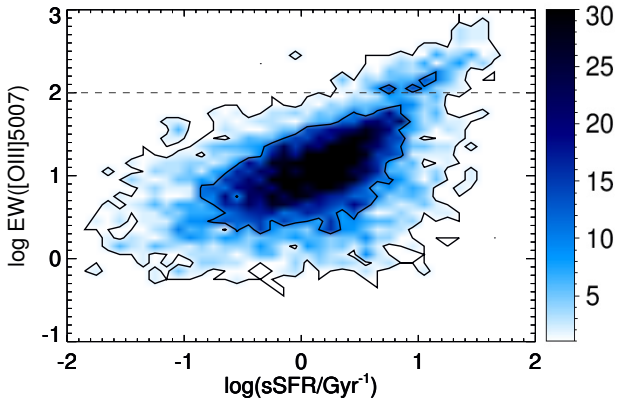


**Fig. 1.** [O III] $\lambda$5007 equivalent width as a function of specific SFR for 5056 galaxies at redshift $0.1 < z < 0.94$ in the SFG-20k sample of Pérez-Montero et al. (2013). The inner and outer contours enclose 68% and 99% of the sample, respectively. The black dashed line delimits our selection threshold, $EW$(O III) ≥ 100 Å, above which galaxies in the zCOSMOS 20k sample are considered to be EELGs.

There are several reasons for the [O III]-based selection of EELGs. Given the spectral range of our VIMOS data and the rest wavelength of [O III], a selection criterion based on this line is more convenient compared to other strong lines (e.g., H$\alpha$ or [O II]) if one intends to maximize the redshift range to be explored using zCOSMOS data. Thus, we are able to collect EELGs on a large redshift range, $0.11 \leq z \leq 0.93$.

In Fig. 1 we show the relation between the *specific* SFR and the rest-frame [O III] equivalent widths of the SFG-20k sample of Pérez-Montero et al. (2013). Despite the relatively large scatter, we find a clear trend with large sSFR galaxies showing higher EWs. Therefore, our selection limit in the EW[O III] for the EELGs guarantees that all these EELGs are among the most efficient SFGs out to $z \sim 1$.

Moreover, it is worth noting that our [O III] criterion also leads us to select galaxies with strong oxygen lines, and with unusually strong hydrogen emission lines and extremely faint and flat continuum. This is shown in Fig. 2, where we compare the H$\alpha$, H$\beta$, [O II], and [O III] EW distribution of both EELG and SFG-20k samples. Clearly, our limit in $EW$([O III]) ≥ 100 Å also leads to the selection of galaxies with very high $EW$(H$\alpha$) ≳ 100 Å and $EW$(H$\beta$) ≳ 20 Å. According to population synthesis models, these limits are an indication of young star formation (<10 Myr; Leitherer et al. 1999) and they have been considered in the literature as a powerful tool with which to select young metal-poor starbursts (e.g., HII galaxies; Sánchez Almeida et al. 2012). An alternative selection criterion based on other strong emission lines would have the drawback that we could only select a smaller number of galaxies over a smaller redshift range, e.g., H$\alpha$ emitters can be selected at $z \lesssim 0.5$.

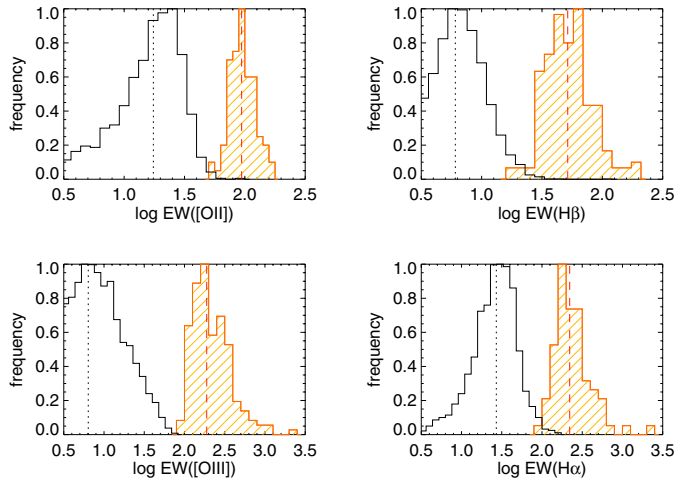


**Fig. 2.** Distribution of rest-frame equivalent widths for the most luminous hydrogen and oxygen emission lines. Black open histograms correspond to the SFG-20k sample, while the red lined histograms correspond to the EELG sample. Dashed and dotted lines indicate median values. The adopted EELG selection criteria include galaxies with the highest EWs in all the observed strong emission lines.

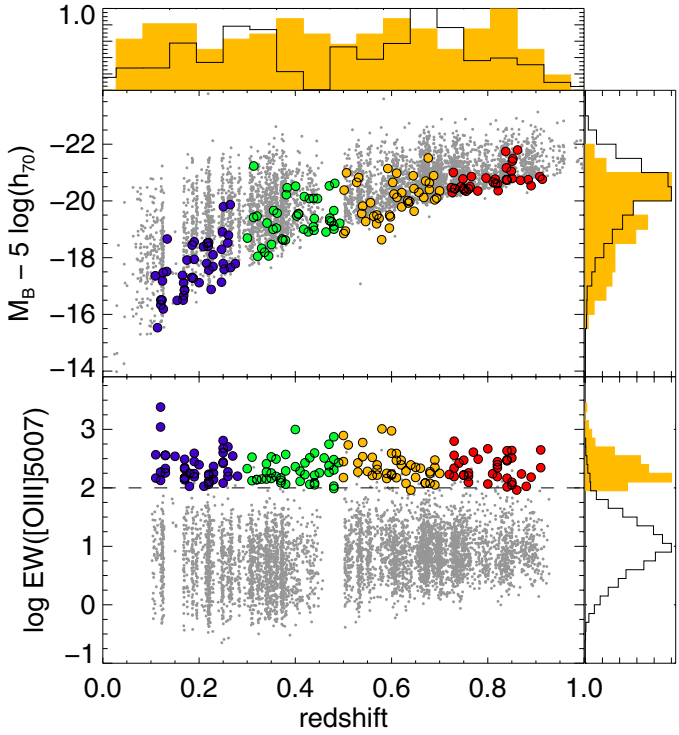


**Fig. 3.** *Two large panels*: rest-frame *B*-band absolute magnitude (above) and rest-frame [O III] equivalent width (below) of the EELGs (large circles) and SFGs (small dots) in zCOSMOS, as a function of redshift. *Upper panel* and *two small panels on the right*: normalized distribution of EELGs (yellow histogram) and SFG (black histogram) in zCOSMOS for these three quantities. The color code denotes bins of redshift: $0.11 \le z \le 0.30$ (purple), $0.30 < z \le 0.50$ (green), $0.50 < z \le 0.70$ (yellow), and $0.50 < z \le 0.93$ (red). The black dashed line delimits our selection threshold, $EW(\mathrm{O\,III}) \ge 100$ Å, above which galaxies in the zCOSMOS 20k sample are considered to be EELGs.

Finally, the choice of a sample of strong [O III] emitters has also been motivated by the aim of collecting a representative and statistically significant sample of star-forming galaxies that would be easily detectable at higher redshifts ($z \sim 2-3$) in deep wide-field NIR surveys (e.g., van der Wel et al. 2011; Atek et al. 2011; Xia et al. 2012; Guaita et al. 2013; Maseda et al. 2013, 2014). Since they would be affected by similar biases, our sample is intended to offer a valuable benchmark for future direct comparison with other probes of strong emission-line galaxies at higher redshifts.

Most of the selected galaxies are faint, with $I_{\mathrm{AB}}$ magnitudes of about ~22 mag. This can make the measurement of their continuum and faint emission-lines relatively uncertain when done with automatic procedures. In order to double check the fluxes and EWs of our EELG sample we have re-measured by hand (using the *splot* task in IRAF) all their emission lines to be sure of their values. Uncertainties on the line fluxes have been computed following Pérez-Montero & Díaz (2003). After discarding a few spurious cases (i.e., extremely noisy spectra or with some defects) we finally define a total sample of 183 EELGs.

Figure 3 shows the distribution of rest-frame absolute magnitude $M_B$ and [O III] EW with redshift for both the EELG and SFG-20k samples. The selected EELGs are approximately uniformly distributed in redshift out to $z \sim 1$ and, by construction, they have the largest EWs. Figure 3 shows that this property also leads us to preferentially select low-luminosity galaxies in the *B* band, including most of the less luminous SFGs in zCOSMOS. The *B*-band luminosity of EELGs spans a wide range, $-16 \lesssim M_B \lesssim -21.5$, and increases with redshift following the same trend as the SFG-20k sample.

### 2.3. Identification of AGNs: diagnostic diagrams

In order to distinguish between purely and non-purely star-forming galaxies in the EELGs sample, we need to identify narrow-line (NL) AGNs (Seyfert 2 and LINERs) because broad-line AGNs were previously excluded from the sample in the selection process. To that end, we use the combination of four empirical diagnostic diagrams based on different bright emission-line ratios, which are presented in Fig. 4. In addition, we cross-correlate our sample galaxies with the XMM and *Chandra* X-rays catalogs from COSMOS (Hasinger et al. 2007; Elvis et al. 2009).

For 63 EELGs at $z \lesssim 0.48$, and depending on the set of lines with available and reliable measurements, we use both the well-known diagnostic diagram (e.g., Baldwin et al. 1981; Veilleux & Osterbrock 1987) based on the line ratios [O III]/H$\beta$ and [N II]/H$\alpha$ (Fig. 4a), and the H$\alpha$ classification proposed by Lamareille (2007) based on [N II], [S II], and H$\alpha$ emission-line ratios (Fig. 4b). For 95 EELGs galaxies with $z > 0.48$, the H$\alpha$, [N II] 6584, and [S II] 6717, 6731 emission lines are no longer visible in the zCOSMOS VIMOS spectra and therefore the above diagnostics cannot be used. Instead, for these galaxies we use the diagnostic diagram defined in Lamareille et al. (2004), involving the [O III]/H$\beta$ and [O II]/H$\beta$ emission-line ratios, as shown Fig. 4c. This diagnostic diagram includes the corrections proposed by Pérez-Montero et al. (2013) to minimize the impact of reddening effects due to the long wavelength baseline between [O II] 3727 and H$\beta$. Finally, for the entire EELG sample we use the empirical MEx diagram (Juneau et al. 2011), where SFGs and AGNs are distinguished by their stellar mass and excitation level (Fig. 4d). Galaxies clearly located above the empirical limits shown in Fig. 4 should be considered AGN candidates.

Overall, the agreement between the first three diagnostics and the MEx diagram is good. Similar results, although with

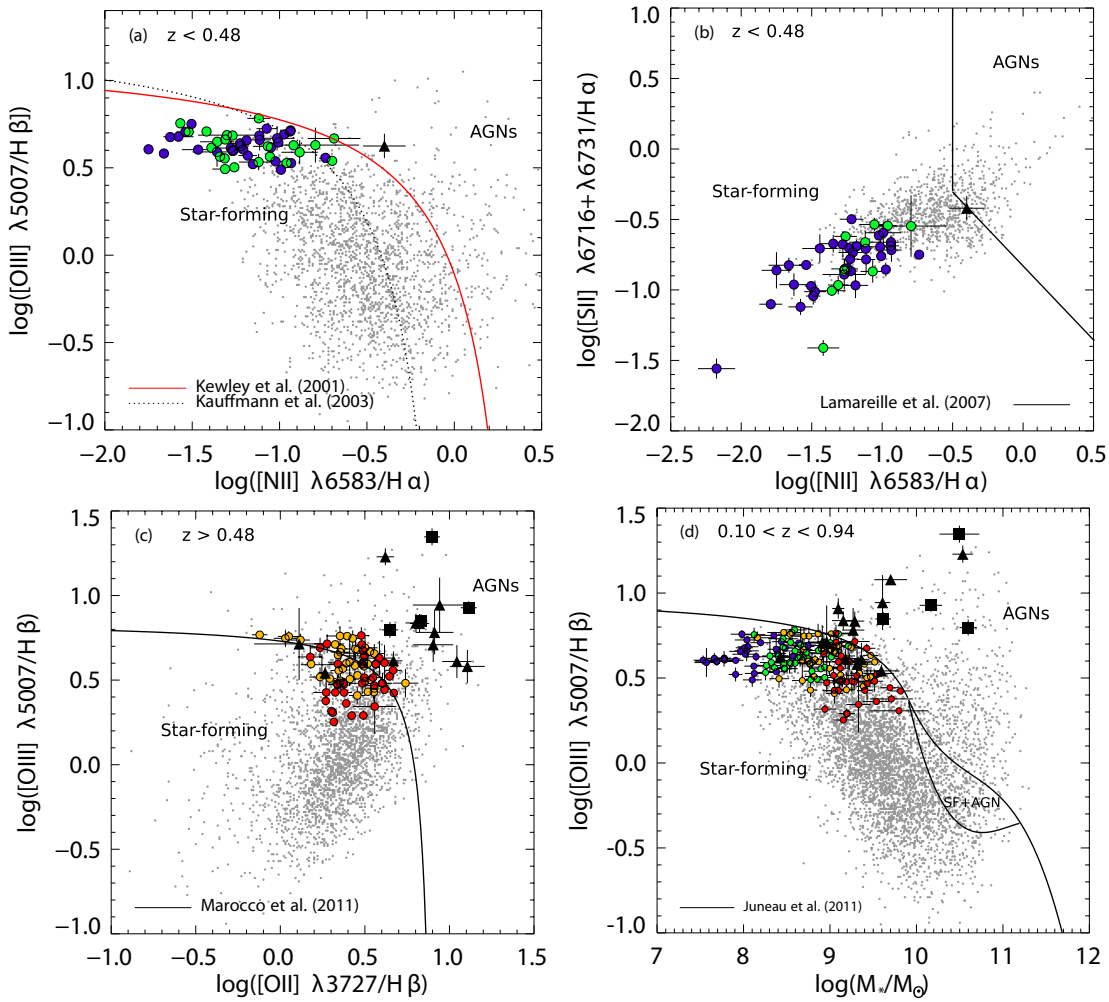


**Fig. 4.** Diagnostic diagrams for EELGs. Large symbols indicate purely star-forming systems (colored) and AGN candidates (black). Small gray dots show galaxies from the SFG-20k parent sample. Colors are as in Fig. 3 and labels indicate the redshift of each subset of galaxies. AGN candidates include both galaxies with detected X-ray counterparts (squares) and galaxies with broad Balmer line components and/or high-ionization emission lines (triangles). Lines show the empirical separation between SFGs and AGNs.

slightly larger dispersion, are found using alternative diagnostics, such as excitation vs. $U - B$ color (Yan et al. 2011). Nonetheless, the above empirical limits typically have $1\sigma$ uncertainties of about 0.2 dex and many EELGs are located very close to these boundaries. This can make the distinction between SFGs and AGNs somewhat tricky for some objects. As an additional test to select AGN candidates we have checked them one-by-one for the presence of X-ray counterparts and bright high-ionization emission lines (e.g., [NeV]), and/or very extended Balmer line components, which can be indicative of the presence of AGNs.

Only four EELGs, all of them at $z > 0.47$, are confirmed X-ray sources (zCOSMOS IDs 819469, 825103, 839230, and 841281). All of them are also clear AGN candidates in the optical diagnostics. The remaining AGN candidates without X-ray counterparts show high-ionization lines such as [NeV] and HeII or unusually broad components in their Balmer lines, and they are typically redder than the rest of the EELGs. In Fig. 5 we present one example of a VIMOS spectrum for both a purely star-forming EELG and a NL-AGN candidate with an X-ray counterpart.

To summarize, using the above criteria, our analysis finds 165 purely star-forming EELGs (90%) and 18 EELGs (10%) with likely NL-AGN contribution.

## 3. The properties of extreme emission-line galaxies in zCOSMOS

In Table 1[2] we present the sample of 165 star-forming EELGs, including fluxes and uncertainties for the most relevant emission lines. These quantities, along with an exquisite multiwavelength dataset, have been used to derive their main properties. In this section we will describe the methodology and briefly discuss our results. A catalog of the most relevant properties for each galaxy is presented in Table 2[2]. The sample has been divided into four redshift bins to further examine possible trends in their main properties with redshift. These bins are almost equally populated and they can be distinguished by color in our figures. Finally, in Table 3 we show median values and standard deviations of the main properties of EELGs according to the defined redshift bins, their optical morphology and their environment. The median properties of the NL-AGN candidates are also included in Table 3. However, the subset of NL-AGN candidates is not considered for the subsequent analysis.

[2] A preview table is shown. A complete version of this table is available at the CDS.

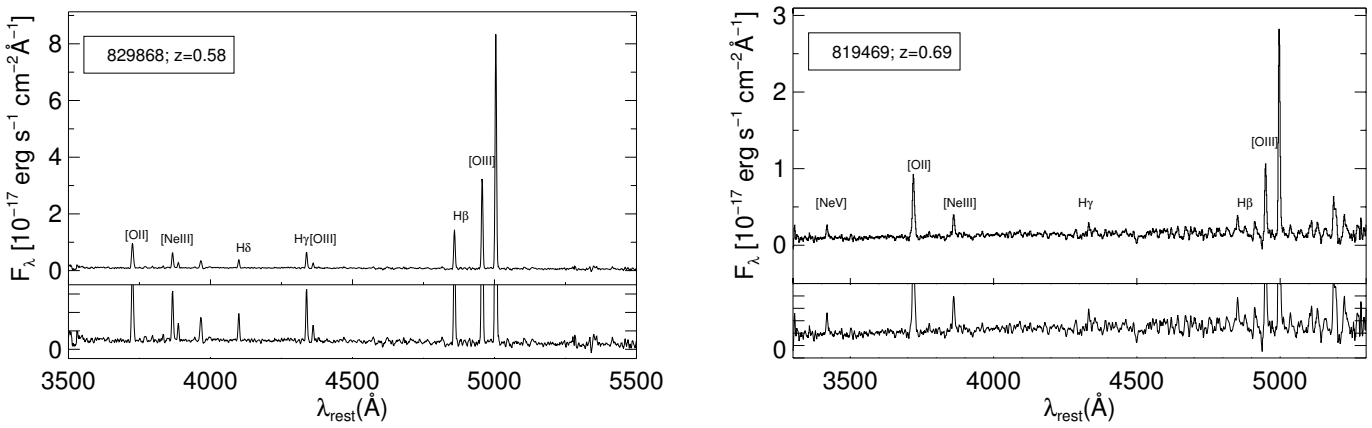


**Fig. 5.** VIMOS spectrum of a purely star-forming (*left*) and a NL-AGN candidate (*right*). The spectra have been smoothed by a two-pixel boxcar filter. The zCOSMOS ID number, the spectroscopic redshift, and the main emission lines are labeled.

### 3.1. The low stellar masses of EELGs

Total stellar masses, $M_*$, for SFGs in the zCOSMOS 20k sample are taken from Bolzonella et al. (2010). They were derived by fitting stellar population synthesis models to both the broadband optical/near-infrared (CFHT: $u, i, Ks$; Subaru: $B, V, g, r, i, z$ Capak et al. 2007) and infrared (*Spitzer*/IRAC: 3.6 $\mu$m, 4.5 $\mu$m Sanders et al. 2007) photometry using a chi-square minimization for each galaxy. The different methods used to compute stellar masses, based on different assumptions about the population synthesis models and the star formation histories, are described in detail in Bolzonella et al. (2010). The accuracy of the photometric stellar masses is satisfactory overall, with typical dispersions due to statistical uncertainties and degeneracies of the order of 0.2 dex. The addition of secondary bursts to a continuous star formation history produces systematically higher (up to 40%) stellar masses, while population synthesis models taking into account the TP-AGB stellar phase (Maraston 2005) produces systematically lower $M_*$ by 0.10 dex. The uncertainty on the absolute value of $M_*$ due to assumptions on the initial mass function (IMF) is within a factor of 2 for the typical IMFs usually adopted in the literature. In this paper, we have adopted stellar masses calculated on the basis of a Chabrier (2003) IMF and the stellar population models of Bruzual & Charlot (2003), with the addition of secondary bursts to the standard declining exponential star formation history.

For strong emission line galaxies a significant contribution to the broadband flux densities from nebular emission is superimposed on the stellar spectral energy distribution (SED). Since standard stellar population synthesis models do not include nebular emission this may have an impact on the SED fitting and, in particular, on the computed total stellar masses (e.g., Krueger et al. 1995; Papaderos et al. 1998; Schaerer & de Barros 2009; Atek et al. 2011; Curtis-Lake et al. 2013; Stark et al. 2013; Castellano et al. 2014; Santini et al. 2015; Pacifici et al. 2015). In order to overcome this potential systematic effect for the sample of EELGs, an additional set of fits were computed after removing the contribution of emission line fluxes to the observed broadband magnitudes. For the models we follow the prescriptions described above for the standard zCOSMOS SED fitting (Bolzonella et al. 2010), but fixing the metallicity of the stellar population models (from $Z = [0.02, 0.2, 0.4, 1]\,Z_\odot$) to the nearest available value to the observed gas-phase metallicity of each galaxy (see Sect. 3.6). In those cases where the gas-phase metallicity was not measured we adopted the median metallicity of the full sample as a reference value.

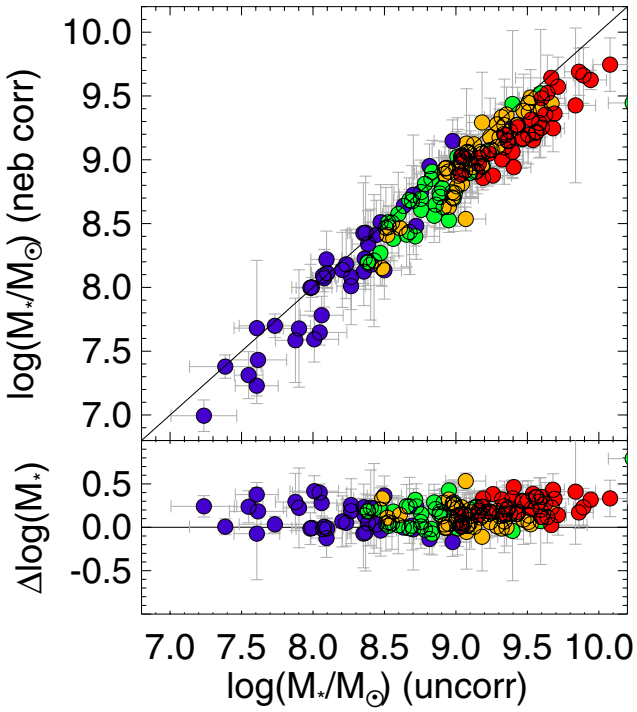


**Fig. 6.** Comparison of stellar masses derived from SED fitting before (uncorr, $x$-axis) and after (nebcorr, $y$-axis) removing the contribution of emission line fluxes to the broadband photometry. *Bottom panel*: difference in stellar mass (uncorr–nebcorr) on the $y$-axis. Symbols and colors are as in Fig. 3.

In Fig. 6 we show a comparison between the stellar masses derived before and after removing the contribution of the strong emission lines. We find the stellar masses derived from SED fitting using uncorrected magnitudes systematically offset to higher values (~0.25 dex in the median) compared to the masses derived from SED fitting after correction for nebular emission. In the most extreme cases (i.e., very high EWs and very low metallicity) neglecting nebular emission in SED fitting may lead to an overestimation of the stellar mass of up to a factor of ~3−5. This result is in good agreement with previous findings for strong emission line galaxies at low and high redshift (e.g., Atek et al. 2011; Curtis-Lake et al. 2013).

In Table 2 we include the stellar masses corrected for nebular emission, which are adopted for the subsequent analysis. Median

**Table 1.** Emission-line fluxes.

| zCOSMOS ID | $\alpha$(J2000) | $\delta$(J2000) | $z$ | [O II] 3727 | H$\gamma$ | [O III] 4363 | H$\beta$ | [O III] 4958 | [O III] 5007 | H$\alpha$ | [N II] 6584 | [S II] 6716 | [S II] 6730 |
|---|---|---|---|---|---|---|---|---|---|---|---|---|---|
| 700882 | 150.349518 | 2.275816 | 0.464 | ... | 1.0 ± 0.3 | ... | 1.9 ± 0.4 | 3.5 ± 0.5 | 9.5 ± 0.6 | ... | ... | ... | ... |
| 701051 | 149.856964 | 2.245983 | 0.345 | ... | 2.3 ± 0.3 | ... | 6.1 ± 0.5 | 8.0 ± 0.6 | 23.9 ± 0.6 | 26.5 ± 0.4 | ... | ... | ... |
| 701741 | 150.393982 | 2.578904 | 0.504 | 9.2 ± 1.0 | 2.2 ± 0.5 | 0.6 ± 0.2 | 4.5 ± 0.3 | 5.5 ± 0.5 | 14.1 ± 0.9 | ... | ... | ... | ... |
| 800984 | 150.286469 | 1.623921 | 0.595 | 7.5 ± 0.5 | 3.4 ± 0.3 | 0.9 ± 0.2 | 9.5 ± 1.0 | 20.5 ± 0.8 | 53.0 ± 1.0 | ... | ... | ... | ... |
| 801094 | 150.242004 | 1.610143 | 0.546 | 6.0 ± 0.3 | 1.3 ± 0.2 | ... | 2.5 ± 0.5 | 2.9 ± 0.3 | 9.6 ± 0.3 | ... | ... | ... | ... |
| 802275 | 149.711777 | 1.616209 | 0.635 | 5.1 ± 0.2 | 0.7 ± 0.1 | ... | 2.0 ± 0.1 | 2.6 ± 0.1 | 6.1 ± 0.2 | ... | ... | ... | ... |
| 803226 | 150.705399 | 1.716969 | 0.570 | 8.5 ± 0.8 | 2.3 ± 0.1 | 0.6 ± 0.2 | 4.5 ± 0.5 | 8.8 ± 0.6 | 25.7 ± 0.8 | ... | ... | ... | ... |
| 803892 | 150.526794 | 1.787344 | 0.439 | ... | 2.0 ± 0.3 | ... | 3.9 ± 0.3 | 4.5 ± 0.4 | 15.0 ± 0.2 | 6.8 ± 1.0 | ... | ... | ... |
| 804130 | 150.452408 | 1.632364 | 0.429 | ... | 1.3 ± 0.2 | ... | 5.4 ± 0.3 | 9.3 ± 0.2 | 25.2 ± 0.3 | 5.9 ± 0.5 | 1.2 ± 0.4 | ... | ... |
| 804791 | 150.286530 | 1.633338 | 0.603 | 13.9 ± 0.3 | 2.7 ± 0.2 | ... | 5.7 ± 0.4 | 7.0 ± 0.3 | 18.2 ± 0.5 | ... | ... | ... | ... |

**Notes.** Measured emission-line fluxes are given in units of $10^{-17}$ erg s$^{-1}$ cm$^{-2}$. Flux errors have been derived following Pérez-Montero & Díaz (2003). No extinction correction has been applied to these fluxes. The entire version of this table for the full sample of EELGs is available at the CDS.

values for each redshift bin are also listed in Table 3. Finally, in Fig. 7b we show the redshift distribution of $M_*$ for EELGs and SFGs in zCOSMOS; Fig. 7b also includes the limiting mass for the SFG-20k sample as derived by Pérez-Montero et al. (2013). We note that EELGs are clearly among the less massive SFGs in zCOSMOS. Their stellar masses are found to increase slowly with redshift, from $\sim 10^7$ at $z \sim 0.1$ to $\sim 10^{10}$ $M_\odot$ at $z \sim 0.9$. Most EELGs are found between the 25% and 75% completeness limit. Therefore, the EELG sample is in a range of masses where the zCOSMOS 20k sample is not complete.

### 3.2. Dust extinction and star formation rate of EELGs

We derive SFRs using the luminosity of the brightest available Balmer emission line after correction for aperture effects and reddening. Aperture effects were quantified using factors derived from photometry[3]. A reddening correction was carried out using the Balmer decrement for those objects with more than one Balmer hydrogen recombination line with $S/N > 2$ available (see Tables 1 and 2), and assuming the theoretical ratios at standard conditions of temperature and density from Storey & Hummer (1995) and the Cardelli et al. (1989) extinction law. Although gas extinction is preferable to be used whenever possible, for a number of galaxies where only one Balmer line is available (~9% of the EELGs and ~36% of the SFG-20k sample), we considered a reddening coefficient from the stellar $E(B-V)$ parameter derived from the stellar synthesis fitting, assuming that the gas and the stellar reddening coefficients are correlated (Calzetti et al. 2000). The same rule was applied for ~32% of the EELGs where the line ratios H$\alpha$/H$\beta$ or H$\beta$/H$\gamma$ were lower than their theoretical values, $(\mathrm{H}\alpha/\mathrm{H}\beta)_0 = 2.82$ and $(\mathrm{H}\gamma/\mathrm{H}\beta)_0 = 0.47$, assuming Case B recombination for typical values of both electron temperature and density[4]. The reddening coefficients, $c(\mathrm{H}\beta)$, for the sample of EELGs are listed in Table 2 and its histogram distribution is presented in Fig. 8. Overall, most galaxies show relatively low dust extinction, with a median reddening of $E(B-V) = 0.19$ mag.

We derive the ongoing star formation rates from extinction-corrected H$\alpha$ luminosities and using the standard calibration of Kennicutt (1998), $SFR(\mathrm{H}\alpha) = 7.9 \times 10^{-42}\, L(\mathrm{H}\alpha)$ [erg s$^{-1}$], which assumes a Salpeter IMF from 0.1 to 100 $M_\odot$. We have scaled down these SFRs by a factor of 1.7 to be consistent with the Chabrier IMF used in this paper. For those galaxies at $z \gtrsim 0.47$ for which H$\alpha$ is not observed in the VIMOS spectra, we derive the expected H$\alpha$ luminosity based on the H$\beta$ fluxes and the assumed theoretical ratio[4], $(\mathrm{H}\alpha/\mathrm{H}\beta)_0 = 2.82$.

We find that EELGs span a large range of $SFR \sim 0.1$–$35$ $M_\odot$ yr$^{-1}$, with median values increasing with redshift, as shown in Fig. 7a and in Table 3. These high SFRs in combination with their low stellar masses imply that EELGs include the most efficient star-forming galaxies of zCOSMOS in terms of specific SFR. This is shown in Fig. 7c, where the sSFR of EELGs does not evolve with redshift and shows a median value of $\log(\mathrm{s}SFR) \sim 0.81\,\mathrm{Gyr}^{-1}$. The extremely high sSFRs of EELGs imply that they are rapidly building up their stellar components. Their stellar mass doubling times (i.e., 1/s$SFR$, or the time needed to double their total stellar mass at their current SFR) are typically a few hundreds million years.

[3] ACS-HST photometry was used if available, Subaru photometry if not.

[4] We assume the theoretical coefficients of Storey & Hummer (1995) for $T_e = 2 \times 10^4$ K and $n_e = 100$ cm$^{-3}$.

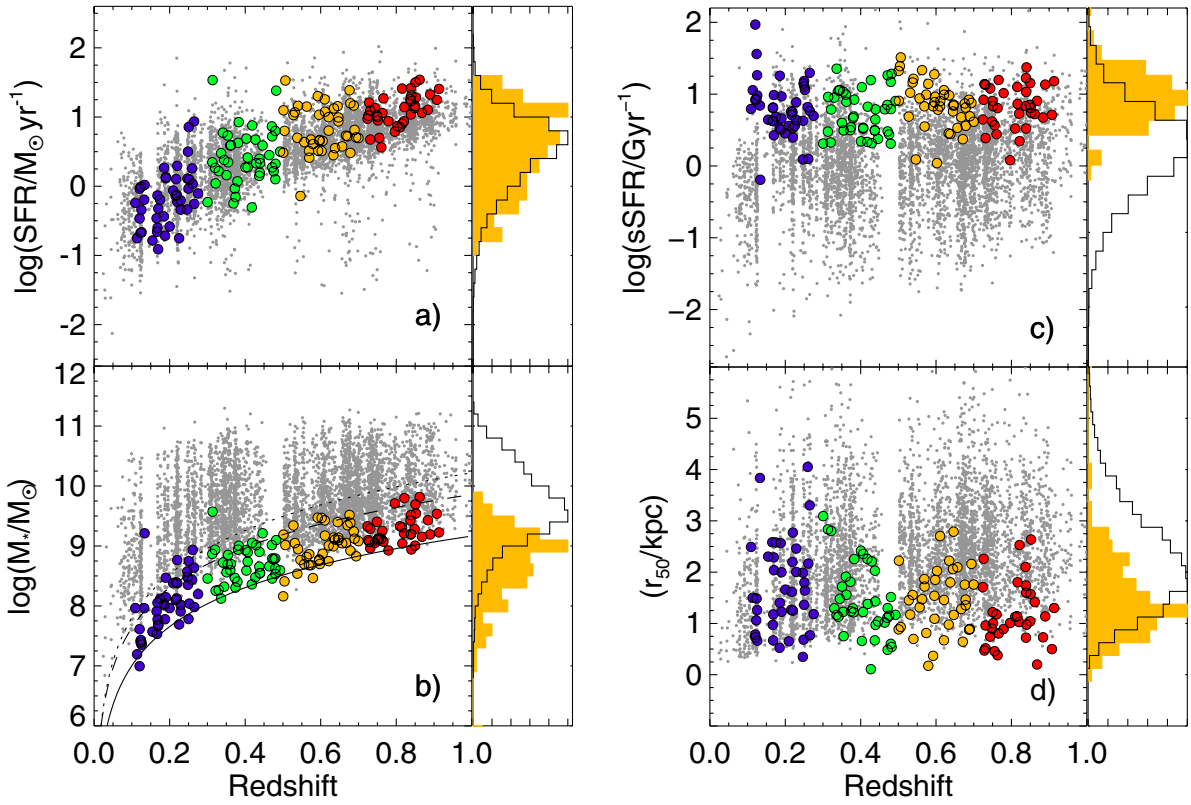


**Fig. 7.** Redshift distributions of SFR **a)**, stellar mass **b)**, specific SFR **c)**, and HST-ACS $I$-band half-light radii **d)**. Symbols and colors are the same as in Fig. 3. The normalized distribution of EELGs (filled) and SFGs (black) for each property are shown in the histograms to the right of the panels. Solid, dashed, and dotted lines in **b)** show the logarithmic fitting to the limiting masses of the star-forming sample for levels 25%, 50%, and 75% of completeness, respectively. The EELGs are small galaxies forming the low end of stellar mass and the high end of sSFR distributions of SFGs in zCOSMOS up to $z \sim 1$.

**Table 2.** Derived properties of EELGs in zCOSMOS.

| zCOSMOS ID | MT | $M_B$ mag | log $L_{FUV}$ $L_\odot$ | $r_{50}$ kpc | log $M_*$ $M_\odot$ | log $SFR_{H\alpha,H\beta}$ $M_\odot$ yr$^{-1}$ | $c(H\beta)$ | 12 + log(O/H) | Method |
|---|---|---|---|---|---|---|---|---|---|
| (1) | (2) | (3) | (4) | (5) | (6) | (7) | (8) | (9) | (10) |
| 700882 | T | –18.9 | 10.23 | 1.02 | $8.66 \pm 0.12$ | $0.45 \pm 0.18$ | $0.28 \pm 0.18^b$ | ... | ... |
| 701051 | T | –18.06 | 9.88 | 1.48 | $8.32 \pm 0.11$ | $0.38 \pm 0.03$ | $0.59 \pm 0.04^a$ | ... | ... |
| 701741 | ... | –18.94 | 10.15 | ... | $8.41 \pm 0.05$ | $0.8 \pm 0.11$ | $0.12 \pm 0.11^b$ | $7.46 \pm 0.15$ | $T_e$ |
| 800984 | T | –19.04 | 10.5 | 1.54 | $8.76 \pm 0.01$ | $1.03 \pm 0.07$ | $0.36 \pm 0.07^c$ | $7.95 \pm 0.07$ | $T_e$ |
| 801094 | ... | –19.27 | 10.29 | ... | $8.77 \pm 0.17$ | $-0.14 \pm 0.13$ | $0.17 \pm 0.13^b$ | $8.14 \pm 0.1$ | $R23$ |
| 802275 | M | –19.93 | 10.7 | 2.22 | $9.14 \pm 0.06$ | $1.13 \pm 0.08$ | $0.54 \pm 0.08^c$ | $8.18 \pm 0.06$ | $R23$ |
| 803226 | C | –19.5 | 10.13 | 1.72 | $8.86 \pm 0.19$ | $0.41 \pm 0.07$ | $0.20 \pm 0.07^b$ | $7.87 \pm 0.1$ | $T_e$ |
| 803892 | C | –18.96 | 9.96 | 1.43 | $8.55 \pm 0.23$ | $0.19 \pm 0.09$ | $0.24 \pm 0.09^b$ | ... | ... |
| 804130 | M | –20.08 | 9.98 | 2.21 | $9.01 \pm 0.07$ | $0.33 \pm 0.16$ | $0.45 \pm 0.09^c$ | $8.53 \pm 0.12$ | $N2$ |
| 804791 | C | –20.65 | 11.05 | 2.02 | $9.47 \pm 0.05$ | $0.51 \pm 0.06$ | $0.05 \pm 0.06^b$ | $8.29 \pm 0.16$ | $R23$ |

**Notes.** Columns: (1) zCOSMOS identification number; (2) morphological type: ($R$) Round/Nucleated, ($C$) Clumpy/Chain, ($T$) Cometary/Tadpole, ($M$) Merger/Interacting; (3) rest-frame absolute $B$-band magnitude. Median $1\sigma$ uncertainties are ~0.07 mag; (4) rest-frame, dust-corrected FUV luminosity. Median $1\sigma$ uncertainties are ~0.11 dex; (5) circularized effective radius. Median $1\sigma$ uncertainties are ~10%; (6) stellar mass from SED fitting (Chabrier 2003 IMF); (7) star formation rate from H$\alpha$ or H$\beta$ luminosity (Chabrier 2003 IMF); (8) reddening constant derived from $^{(a)}$ H$\alpha$/H$\beta$ or $^{(b)}$ H$\gamma$/H$\beta$ ratios, whenever possible, or $^{(c)}$ the SED best-fitting for those galaxies where $^{(a)}$ and $^{(b)}$ cannot be measured or where they produce a negative extinction (i.e., H$\alpha$/H$\beta$ < 2.82 or H$\gamma$/H$\beta$ < 0.47, assuming Case B recombination with $T_e = 2 \times 10^4$ K, $n_e = 100\,\mathrm{cm}^{-3}$); (9) gas-phase metallicity. The uncertainties quoted for 12+log(O/H) only take into account the propagation of errors from the emission line flux measurements; (10) method used for metallicity derivation (see text for details). The entire version of this table for the full sample of EELGs is available at the CDS.

#### 3.2.1. UV properties

Galaxy Evolution Explorer (GALEX) data in the far-ultraviolet (FUV, $\lambda_c \sim 1530$ Å) and near-ultraviolet (NUV, $\lambda_c \sim 2315$ Å) from the COSMOS/GALEX photometric catalog (Schiminovich et al. 2007; Zamojski et al. 2007) were used to derive rest-frame UV luminosities and colors for most of the EELGs. We calculate rest-frame FUV absolute magnitudes consistently with those in the optical and IR used for the SED fitting and stellar mass derivation (Bolzonella et al. 2010). In order to account for intrinsic dust attenuation, we have adopted the relation between the total dust attenuation and UV spectral slope given

**Table 3.** Median properties of zCOSMOS EELGs.

| Subsample | $N$ | $z$ | $M_B$ | $c(H_\beta)$ | $r_{50}$ | $\beta_{UV}$ | $\log L_{FUV}$ | $SFR_{H\alpha,H\beta}$ | $\log M_*$ | 12+ log(O/H) |
|---|---|---|---|---|---|---|---|---|---|---|
| | | | | | kpc | | $L_\odot$ | $M_\odot\,yr^{-1}$ | $M_\odot$ | |
| | (2) | (3) | (4) | (5) | (6) | (7) | (8) | (9) | (10) | (11) |
| 1 ($0.11 \le z \le 0.30$) | 44 | 0.19 | −17.6 (0.9) | 0.31 (0.19) | 1.6 (1.4) | −1.44 (0.51) | 9.6 (0.5) | 0.6 (2.6) | 8.02 (0.47) | 8.10 (0.23) |
| 2 ($0.30 < z \le 0.50$) | 43 | 0.40 | −19.3 (0.7) | 0.27 (0.18) | 1.3 (1.0) | −1.66 (0.32) | 10.2 (0.3) | 2.2 (2.4) | 8.70 (0.29) | 8.07 (0.22) |
| 3 ($0.50 < z \le 0.70$) | 42 | 0.61 | −20.1 (0.7) | 0.27 (0.16) | 1.5 (0.6) | −1.61 (0.31) | 10.6 (0.3) | 6.3 (2.1) | 9.02 (0.31) | 8.16 (0.19) |
| 4 ($0.70 < z \le 0.93$) | 36 | 0.82 | −20.7 (0.4) | 0.31 (0.15) | 1.0 (0.6) | −1.68 (0.43) | 10.8 (0.2) | 12.7 (1.7) | 9.21 (0.24) | 8.21 (0.17) |
| All-SF | 165 | 0.48(0.23) | −19.5 (1.4) | 0.27 (0.17) | 1.3 (1.0) | −1.61 (0.41) | 10.4 (0.6) | 3.9 (3.9) | 8.79 (1.07) | 8.16 (0.21) |
| All-SF in groups | 48 | 0.35(0.22) | −18.9 (1.5) | 0.31 (0.17) | 1.4 (1.1) | −1.55 (0.43) | 10.3 (0.6) | 2.4 (4.1) | 8.72 (1.08) | 8.15 (0.23) |
| Round/nucleated | 30 | 0.44 (0.25) | −19.1 (1.4) | 0.36 (0.20) | 1.0 (0.3) | −1.54 (0.42) | 10.2 (0.5) | 3.2 (3.6) | 8.54 (1.08) | 8.13 (0.26) |
| Clumpy/chain | 60 | 0.48 (0.23) | −19.5 (1.5) | 0.31 (0.15) | 1.5 (0.7) | −1.61 (0.43) | 10.3 (0.6) | 3.9 (4.3) | 8.76 (1.07) | 8.14 (0.21) |
| Cometary/tadpole | 27 | 0.46 (0.20) | −19.2 (1.4) | 0.27 (0.18) | 1.5 (0.7) | −1.70 (0.36) | 10.3 (0.6) | 3.3 (3.7) | 8.70 (1.07) | 8.08 (0.21) |
| Merger/interacting | 48 | 0.55 (0.23) | −20.2 (1.1) | 0.27 (0.17) | 1.5 (1.5) | −1.55 (0.41) | 10.6 (0.5) | 6.2 (3.7) | 9.05 (1.05) | 8.18 (0.16) |
| NL-AGN | 18 | 0.78 (0.16) | −20.7 (0.8) | 0.62 (0.45) | 1.2 (0.3) | −1.32 (0.83) | 10.9 (0.5) | 17.2 (4.4) | 9.36 (1.10) | – |

**Notes.** Columns: (2) Number of galaxies. (3) to (11) Median (and 1$\sigma$ dispersion) values for: redshift, rest-frame $B$-band absolute magnitude, reddening, circularized half-light radius, UV spectral slope, dust-corrected FUV luminosity, dust-corrected star formation rate, stellar mass, and metallicity.

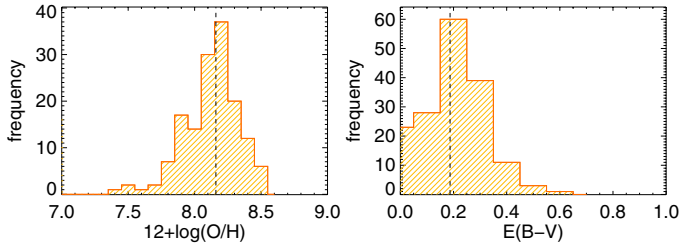


**Fig. 8.** Distribution of gas-phase metallicity (*left*) and reddening (*right*) for the sample of EELGs. Vertical dashed lines indicate median values. The EELGs are low-extinction, metal-poor systems.

by Meurer et al. (1999) for a sample of local starbursts with IR and UV measurements, which can be expressed as $A_{FUV}$ = 4.43+1.99 $\beta_{UV}$. In this equation $\beta_{UV}$ = 2.32 (FUV − NUV)−2.0 is the photometric measurement of the UV spectral slope in rest-frame.

The resulting dust-corrected FUV luminosities, $L_{FUV}$, for each galaxy are listed in Table 2. Median values of $\beta_{UV}$ and $L_{FUV}$ for the various subsets are also included in Table 3. Our EELG sample shows typical values of $\beta_{UV} = -1.61$, which according to the Meurer formula imply dust attenuations of $A_{FUV} \sim 1.23$ mag. This value is ∼30% lower than the one derived from a mean reddening derived from the optical of $E(B-V) \sim 0.2$ assuming a Cardelli et al. (1989) extinction law with $A_{FUV} = 8.15\,E(B-V)$. After dust corrections we find for EELGs median luminosities of $L_{FUV} \sim 10^{10.4}\ L_\odot$ and FUV surface brightnesses[5] of $\mu_{FUV} \gtrsim 10^9\ L_\odot\,kpc^{-2}$. These values mean that the EELGs are very compact and luminous in the UV continuum.

Using dust-corrected FUV luminosities we also derive FUV-based SFRs using the calibration given by Kennicutt (1998), $SFR_{FUV} = 1.4 \times 10^{-28}\,L_{FUV}$ [erg s$^{-1}$ Hz$^{-1}$], scaled down to a Chabrier IMF. In Fig. 9 we compare the SFRs derived from the SED fitting and those from H$\alpha$ and FUV after dust-attenuation corrections. Even though the scatter is relatively large, both $SFR_{H\alpha}$ and $SFR_{FUV}$ are in excellent agreement.

Since $SFR_{FUV}$ traces massive star formation over a longer time scale than H$\alpha$ (typically up to a factor of 10, Kennicutt & Evans 2012), this would imply that these galaxies are experiencing a very recent and probably the first major star formation episode in the last several hundreds million years. We note, however, that compared with the SFR derived from the SED fitting both $SFR_{H\alpha}$ and $SFR_{FUV}$ are systematically lower by ∼0.2 dex, as shown in Fig. 9. This offset can be understood as due to some of the assumptions involved in the derivation of the three SFR tracers. In particular, one of the most critical ones is the dust attenuation correction.

Recent work by Castellano et al. (2014) suggests that for young, low-metallicity galaxies at high redshift the SFRs derived from dust-corrected UV luminosities can be underestimated by up to a factor of 2−10 regardless of the assumed star formation history. Such a discrepancy is due to the solar metallicity implied by the usual $\beta_{UV}$–$A_{FUV}$ conversion factor. Since our EELGs are characterized by their strongly subsolar metallicities, their dust attenuations derived through the Meurer formula might be systematically lower than the true ones and, therefore, the derived $SFR_{FUV}$ might be underestimated. In our study this hypothesis is supported by the fact that the SFR derived from the SED (which takes into account the metallicity of the galaxy to choose the best-fit model) is always systematically offset to higher values

[5] $\mu_{FUV} = \frac{0.5 L_{FUV}}{\pi r_{50}^2}$, where $r_{50}$ is the optical half-light radius (see Sect. 3.4.2).

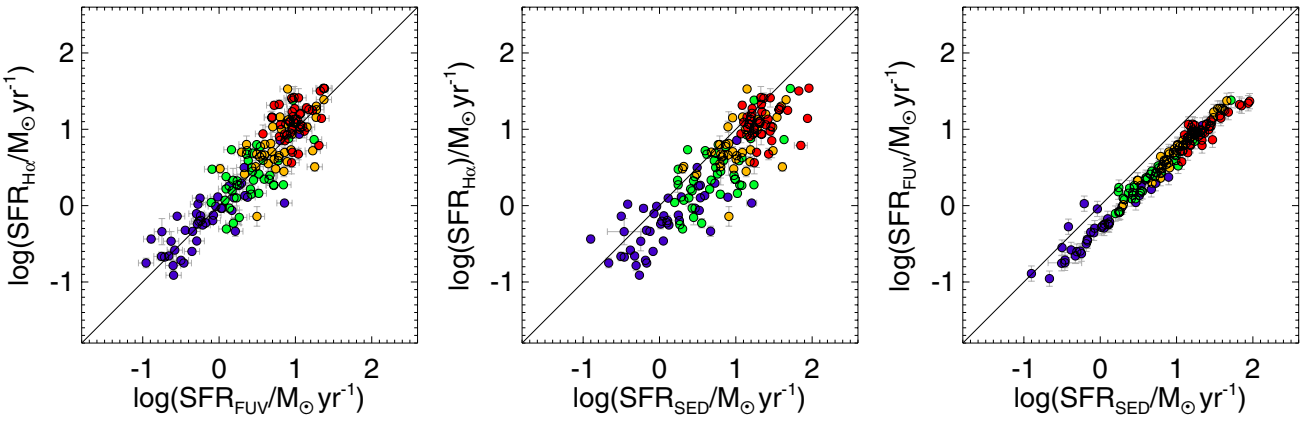


**Fig. 9.** Comparison between star formation rates derived from the SED fitting ($SFR_{SED}$), the extinction-corrected H$\alpha$ luminosity ($SFR_{H\alpha}$), and the rest-frame attenuation-corrected FUV luminosity ($SFR_{FUV}$) for the sample of EELGs. The solid lines indicate the one-to-one relation.

by ∼0.2 dex. In agreement with the results of Castellano et al. (2014) if this offset is only due to the dust attenuation correction it would imply that Meurer's zeropoint should be corrected upwards by this quantity for typical EELGs, resulting in a median dust attenuation in the FUV of about ∼10−20% higher.

Although a rigorous analysis of the discrepancies between different SFR indicators is far from the scope of this paper, we caution about using dust attenuation corrections for low-metallicity galaxies under the assumption of models and calibrations which are valid for solar metallicity environments.

### 3.3. The gas-phase metallicity of EELGs

Given the wide redshift range of the sample, the low S/N of some faint emission lines, and the limited wavelength coverage of the VIMOS spectra, the derivation of gas-phase metallicity in our sample of EELGs cannot be addressed using a unique methodology. Thus, we use four different methods to derive metallicities for 149 out of 165 EELGs (∼90% of the sample) with reliable measurements for the required set of lines imposed by these methods, as described below.

Metallicities and associated uncertainties for the EELGs are presented in Table 2, where we also indicate the method applied in each case. Median values for both redshift bin and morphological type are presented in Table 3.

In Fig. 8 we show the histogram distribution of metallicities for the EELGs. They span a wide range of subsolar values (12+log(O/H) = 7.3−8.5), with a median value of 12+log(O/H) = 8.16 (∼0.18 $Z_\odot$). Moreover, we do not observe a trend in metallicity with redshift. These results are in good agreement with the typical values found for local star-forming galaxies (e.g., HII galaxies and BCDs; Terlevich et al. 1991; Kniazev et al. 2004).

#### 3.3.1. Metallicity derived through the direct method

The direct method (also known as the $t_e$-method) is the most accurate method for deriving the oxygen abundance in star-forming galaxies (e.g., Hägele et al. 2008). It is based on the previous determination of the electron temperature of the gas, using the intensity ratio of nebular-to-auroral emission lines (e.g., [O III]$\lambda\lambda$ 4959,5007 and [O III]$\lambda$ 4363) and the relative intensity of the strongest nebular emission lines to a hydrogen recombination line. Since for the EELGs we do not have a direct estimation of the [O II] electron temperature, they have been derived using the model-dependent relation between the [O III] and [O II] electron temperatures, $t_e$ [O III] and $t_e$ [O II], proposed by Pérez-Montero & Díaz (2003), which takes into account the dependence of $t_e$ [O II] on the electron density. Then, following the expressions in Pérez-Montero & Contini (2009), $O^+$ and $O^{2+}$ have been calculated using $t_e$ [O III] and $t_e$ [O II] and the relative intensities of the corresponding bright emission lines, namely [O II]$\lambda$ 3727 and [O III]$\lambda$ 4363, plus [O III]$\lambda\lambda$ 4959,5007. Finally, $O^+$ and $O^{2+}$ have been combined to estimate the total abundance of oxygen relative to hydrogen, O/H.

Following the direct method we have derived ionic abundances in 26 purely star-forming EELGs (∼16%) uniformly distributed in redshift from $z \sim 0.45$[6] and with reliable measurements ($S/N > 2$) of all the involved emission lines, including [O III]$\lambda$4363. We find direct metallicities spanning a large range of values, 12+ log(O/H) = 7.5−8.4.

#### 3.3.2. Metallicity of EELGs without [O II] measurements: the $t_e$ [O III]-Z calibration

For EELGs with reliable measurements of the [O III] 4363,4959, 5007 lines, but without [O II] line measurement, i.e., those where [O II] lines lie out of the VIMOS spectral range, we cannot derive $O^+$, so we do not have a direct measurement of the metallicity. In our sample, 19 galaxies (∼12%) at $z < 0.48$ fall into this category. For these galaxies, however, we can derive a semi-direct metallicity taking advantage of the tight relation between $t_e$ [O III] and $Z$ expected for high-excitation environments – like those present in EELGs – from both observations and models (e.g., Masegosa et al. 1994; López-Sánchez et al. 2012). Thus, we calibrate the relation between $t_e$ [O III] and $Z$ for EELGs (dubbed hereafter the $t_e$ [O III]−$Z$ calibration) using a combination of two independent datasets. We use metallicities derived using the direct method for both giant HII regions and HII galaxies from Pérez-Montero & Contini (2009) and the sample of green pea galaxies from Amorín et al. (2010). In order to avoid a strong dependence on the ionising parameter, the calibration was restricted to those objects with [O II]/[O III] ratios in the range covered by the EELG sample (Fig. 10a).

In Fig. 10b we show the $t_e$ [O III]−$Z$ calibration, which produces the expression

$$12+\log(O/H) = 9.22\,(\pm0.03) - 0.89\,(\pm0.02)\,t_e[O\,III], \quad (1)$$

[6] The lower limit in redshift is due to the blue cut-off of the VIMOS grism used for the zCOSMOS bright survey, which precludes the observation of [O II]$\lambda$3727 and [O III]$\lambda$4363 at lower redshift.

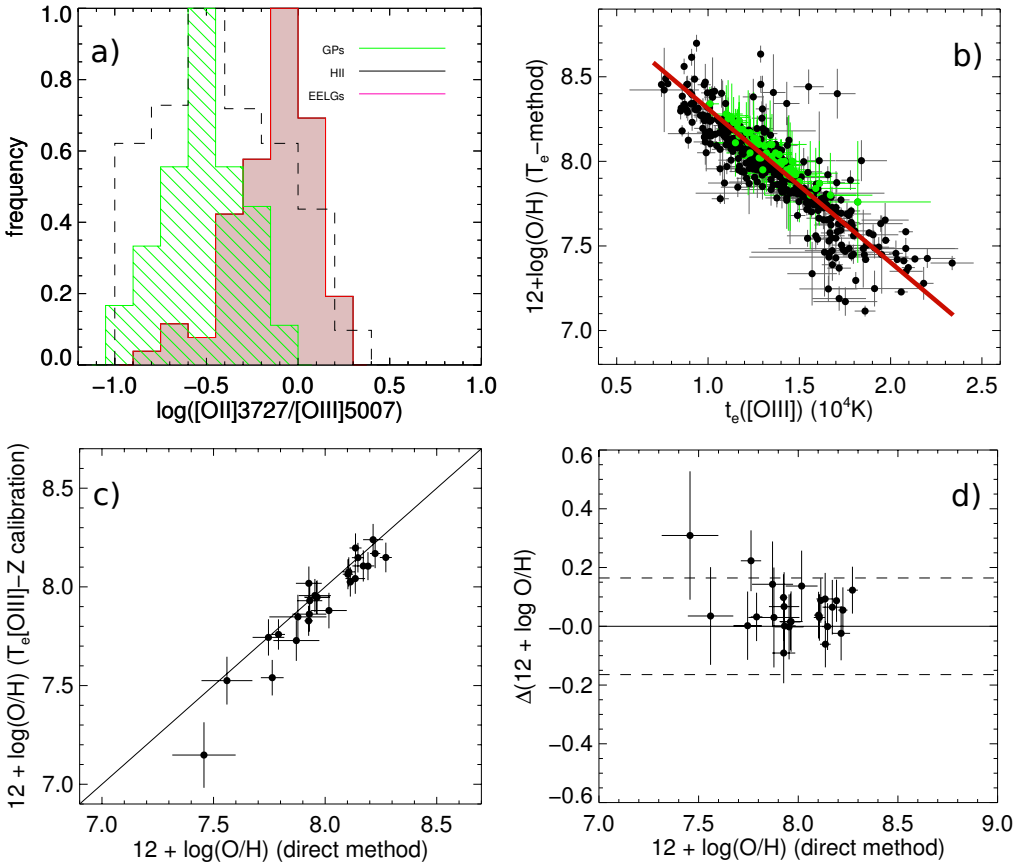


**Fig. 10. a)** Histogram distributions of the ionization parameter, estimated with the [O II]/[O III] ratio, for EELGs, green peas (GPs), and HII galaxies. **b)** Relation between the oxygen abundance derived from the direct method and the [O III] electron temperature, $t_e$[O III], for the sample of giant HII regions and nearby HII galaxies from Pérez-Montero & Contini (2009, black points) and the sample of GPs from Amorín et al. (2010, green points). The red line indicates the best-fit to the data shown in Eq. (1). **c)** Comparison between the metallicity derived using the direct method and from the $t_e$[O III] $-Z$ calibration shown in Eq. (1) and their residuals **d)**. Dashed lines in **d)** indicate the $2\sigma$ limits.

where $t_e$[O III] is the [O III] electron temperature calculated from the [O III] ($\lambda$4959+$\lambda$5007)/$\lambda$4363 ratio in units of $10^4$ K. Uncertainties in the $t_e$ [O III] $-Z$ calibration translate into uncertainties of $\lesssim$0.15 dex ($1\sigma$) in metallicity. As a consistency check, we have applied the $t_e$[O III] $-Z$ calibration to those EELGs with metallicities derived using the direct method.

In Fig. 10c we show that the two metallicity estimates based on the electron temperature are in good agreement over the wide range of metallicity covered by our sample, with deviations broadly consistent within the errors. Only a small shift of $\sim$0.1−0.2 dex is noticed in some cases, especially at lower metallicities, i.e., 12+log(O/H) $\lesssim$ 7.7. In this range, the $t_e$[O III] $- Z$ calibration has a lower statistical significance and the scatter is large, probably because of an increased sensitivity of $t_e$[O III] on the ionization parameter. Therefore, in extremely metal-poor galaxies Eq. (1) should be applied with caution. Moreover, we emphasize that the calibration presented in Eq. (1) is well suited for determining reliable oxygen abundances only in objects with similar (i.e., high) ionization conditions to those shown by the EELGs. Thus, the $t_e$[O III] $-Z$ calibration may appear an alternative for other sa mples of gas-rich galaxies with similar ionization conditions where the limitation in the spectral coverage does not allow a proper determination of the [O II] flux.

### 3.3.3. Metallicity from strong-line methods

The two methods explained in Sects. 3.3.1 and 3.3.2 are based on the determination of the electron temperature and cannot be applied to the whole sample of EELGs either because at certain redshifts the [O III]$\lambda$ 4363 line is not included in the VIMOS spectral range, or because this line is too weak. One alternative for the derivation of the gas-phase metallicity in these galaxies is the use of the so-called strong-line methods. They are based on the direct calibration of the relative intensity of the strongest collisionally excited emission-lines with grids of photoionization models or samples of objects with an accurate determination of the oxygen abundance, or both.

There is a wide variety of strong-line methods used in the literature, which usually give different results depending on the metallicity range, ionization conditions, and available line ratios (see Kewley & Ellison 2008, for an extensive discussion). In order to derive metallicities consistent with those derived from the $t_e$-based methods, here we use three different empirical calibrations based on a sample of nearby objects with accurate determinations of 12+log(O/H) via the direct ($t_e$) method. We use the calibration proposed by Pérez-Montero & Contini (2009) based on the *N2* parameter, defined as the ratio of [N II] $\lambda$ 6584 to H$\alpha$ by Storchi-Bergmann et al. (1994), and used by Denicoló et al. (2002) as a metallicity proxy. This method is our choice for EELGs at $z \lesssim 0.30$, where [N II] and H$\alpha$ are included in the VIMOS spectra but [O III] is not. Although this relation does not present any dependence on reddening correction or on flux calibration uncertainties, *N2* depends on the ionization parameter, the equivalent effective temperature of the ionising cluster, and the nitrogen-to-oxygen ratio (Pérez-Montero & Díaz 2005). Taking these effects into account, in EELGs – which show

homogeneous excitation properties (see Fig. 10) – the overall uncertainty is ∼0.2 dex across their entire metallicity range.

For EELGs at $z > 0.48$ where the [O III] auroral line is too weak to derive $t_e$[O III] and *N2* cannot be applied (i.e., H$\alpha$+[N II] lie out of the spectral range), metallicity is derived using the $R_{23}$ parameter. This parameter is defined as the ratio between the sum of [O II]$\lambda$ 3737 and [O III]$\lambda\lambda$ 4959,5007 to H$\beta$ fluxes (Pagel et al. 1979). The main drawback of $R_{23}$ is its degeneracy with $Z$. Moreover, $R_{23}$ has a strong dependence on the ionization parameter and effective temperature. To minimize this dependence we use the calibration proposed by Kobulnicky et al. (2003), based on the photoionization models from McGaugh (1991), which includes additional terms as a function of [O II]/[O III], a proxy of the ionization parameter. Most of the EELGs are located in the turnover region of the $R_{23}$ calibration. Therefore, for galaxies with a difference of $\lesssim$0.3 dex between the metallicity provided by the upper and lower branches we adopt a mean value as the final metallicity. For galaxies where this difference is higher we adopt the upper branch of the $R_{23} - Z$ relation because we interpret the weakness of the [O III] auroral line in high S/N spectra as a possible indication of high (12+log(O/H) $\gtrsim$ 8.2) metallicities. Nonetheless, we note that we do not find EELGs with 12+log(O/H) > 8.5.

Finally, it is worth mentioning that important differences may arise when using different strong-line methods and/or different calibrations (see, e.g., Kewley & Ellison 2008; Pérez-Montero 2014). Here, metallicities derived using the *N2* calibration of Pérez-Montero & Contini (2009) are consistent with those derived from the direct method. However, the adopted calibration of $R_{23}$ is not based on galaxies with direct metallicities but on grids of photoionization models, which may produce a systematic bias. To overcome these differences, we follow Pérez-Montero et al. (2013) and convert the metallicities derived from $R_{23}$ to those derived from *N2* using the linear relations described in Lamareille et al. (2006b), which are based on models of Charlot & Longhetti (2001). This way, the adopted estimators find metallicities that are broadly consistent, within the uncertainties, with each other.

### 3.4. Diverse morphologies of EELGs

#### 3.4.1. Visual classification

Our first approach to studying the morphological properties of the EELG sample was to perform a visual classification using the available HST/ACS *F814W*-band images from COSMOS. We excluded from the analysis five EELGs that have not been imaged with ACS and are nearly unresolved in ground-based images. Inspired by classical visual classifications of BCDs (e.g., Cairós et al. 2001) we distinguish here four major morphological classes of EELGs according to the distribution and shape of their high- and low-surface-brightness components:

1. *Round/nucleated*: galaxies showing one bright star-forming knot embedded in a nearly symmetric low surface brightness envelope and galaxies with point-like/unresolved appearance. About 18% of EELGs are in this class.
2. *Clumpy/chain*: galaxies with two or more high-surface-brightness knots spread out over a diffuse or asymmetric low-surface-brightness component. These EELGs represent ∼37% of the sample galaxies.
3. *Cometary/tadpole*: galaxies with head-tail shape, where a main bright star-forming clump is located at the head and a low-surface-brightness tail is off to one side. About 16% of the EELGs are in this class.
4. *Merger/interacting*: galaxies with a distorted low-surface-brightness component, features potentially associated with past or current interaction with very close companions, e.g., tails, bridges, etc. These EELGs are about 29% of the sample.

Morphological classes for the sample of EELGs are given in Table 2, while several illustrative examples are shown in Fig. 11. None of the above classes appears to be biased to any redshift bin; all of them show nearly the same median redshift (Table 3). We note that EELGs belonging to the last three morphological classes can be simply considered as "irregular" galaxies. Although there might be an inevitable overlap between them (e.g., some clumpy/chain or cometary/tadpole EELGs may be also interpreted in terms of interactions) a more detailed description of both the distribution of the star-forming regions and the shape of the underlying diffuse component in broadband images remains interesting. In particular, it may be useful to study the possible mechanisms responsible for the origin of the starburst and chemical enrichment in these galaxies (e.g., Papaderos et al. 2008; Filho et al. 2013; Sánchez Almeida et al. 2013, 2014; Amorín et al. 2009) and to compare them with galaxies of similar morphologies identified at higher redshifts (e.g., Elmegreen et al. 2012, 2013; Amorín et al. 2012b).

#### 3.4.2. Quantitative analysis

In addition to our visual classification, we adopt a quantitative classification scheme based on different non-parametric diagnostics of galaxy structures (e.g., Abraham et al. 1996; Conselice 2003; Lotz et al. 2004; Huertas-Company et al. 2008). In short, we use high-resolution imaging in the *F814W* filter from the HST/ACS and the fully automated method developed by Tasca et al. (2009) to derive standard morphological parameters[7], such as half-light radius $R_{50}$ and axial ratio $q = b/a$, concentration index ($C$), asymmetry ($A$), and the Gini coefficient ($G$).

The above parameters are used simultaneously by two different optimized algorithms[7] referred to as INT (Tasca et al. 2009) and SVM (Huertas-Company et al. 2008), to define the boundaries between three predefined morphological classes, early, spiral, and irregular, in an automated and objective way. In Fig. 12 (bottom panels) we show the normalized distributions of SFGs and EELGs in zCOSMOS over these three classes for the two methods. We find that both INT and SVM algorithms provide similar results. While most SFGs in zCOSMOS are classified as spiral, the EELG sample contain a significantly higher fraction of galaxies classified as irregular.

We find a qualitative agreement between the results of the classification schemes shown in Fig. 12 and our visual classification, in the sense that almost all the EELGs in the cometary/tadpole, clumpy/chain, and merger/interacting classes are automatically classified as irregular or spiral, whereas most EELGs classified as round/nucleated are classified as elliptical. Taken together, we conclude that at least ∼80% of the sample presents non-axisymmetric morphologies.

In Fig. 12 we also show the normalized distribution of morphological parameters for the EELG and SFG-20k samples in the same stellar mass range. The EELGs are small systems, with half-light radii[8] $r_{50}$ in a range between ∼0.3 and ∼4 kpc, with

[7] See Tasca et al. (2009) and Huertas-Company et al. (2008) for details on the definition of morphological parameters and on the algorithms adopted for the morphological classification.

[8] We have circularized the measured half-light radii $R_{50}$ as $r_{50} = R_{50}\, q^{0.5}$, where $q$ is the axial ratio $b/a$. Both quantities have been measured from the $I$-band (*F814W*) HST-ACS images.

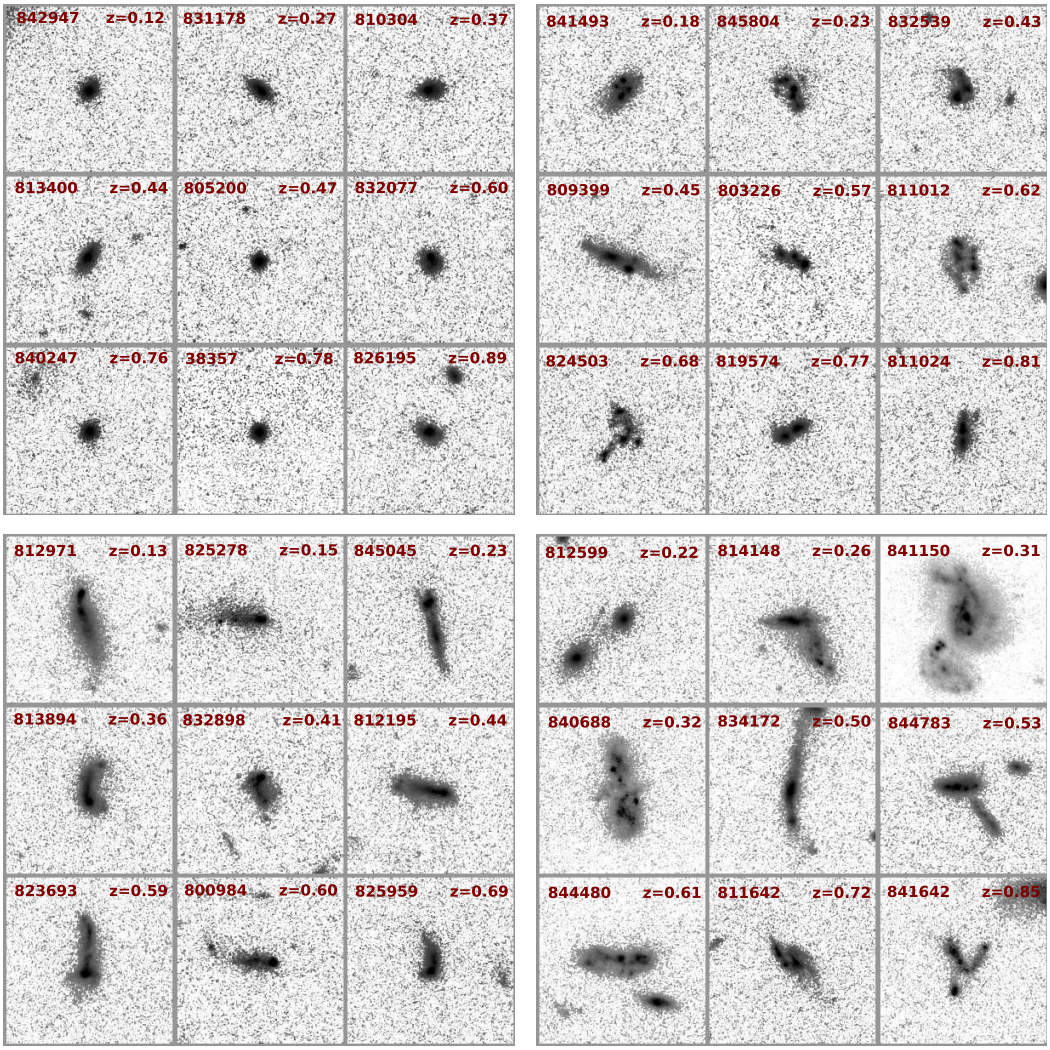


**Fig. 11.** Morphology of star-forming EELGs. Examples of round/nucleated (*upper left*), clumpy/chain (*upper right*), cometary/tadpole (*bottom left*), and merger/interacting (*bottom right*) morphologies from their HST/ACS *I*-band (*F*814*W*) images. The images are oriented to the north–east and are 6″ on a side. The redshift for each galaxy is indicated in the labels.

a median value of 1.3 kpc. Similarly to most galaxies in the SFG-20k sample, the *C*, *A*, and *G* parameters for the EELGs are spread over a wide range of values. However, there is a clear tendency for the EELGs to show larger asymmetry and also higher concentration and Gini parameters than normal SFGs.

The same conclusion arises from Fig. 13, where we show the asymmetry-concentration and asymmetry-Gini diagrams for both zCOSMOS SFGs and EELGs. Especially at low values of C, the EELGs show larger values of A compared to those of normal SFGs at a given *C* or *G*. From Fig. 13 we also test the consistency between the visual and quantitative classifications. Those EELGs visually classified as round/nucleated show higher concentration and Gini parameters than those included in irregular classes. Figure 13 also highlights the difficulty of distinguishing between galaxies with different irregular morphologies, such as cometary or clumpy galaxies on the basis of such quantitative diagrams only.

Among our EELGs we do not find any clear correlation between the morphological properties and other galaxy-averaged properties such as redshift, absolute magnitudes, SFRs, stellar masses, extinction, or gas-phase metallicity. In particular, we do not find significant differences between the median properties of rounded and irregular EELGs (see Table 3).

### 3.5. The environment of EELGs

We study the large-scale environment of the EELG sample using the zCOSMOS 20k group catalog (Knobel et al. 2012). This catalog includes about 16 500 galaxies between $0.1 \lesssim z \lesssim 1$, and contains 1498 groups in total, of which 192 have more than five members. Full details about the catalog can be found in Knobel et al. (2009, 2012).

We cross-match the group catalog and both the SFG-20k and the EELG samples. We find that ~26% of the galaxies in the SFG-20k sample are in groups of two or more spectroscopic members. Similarly, we find 48 out of 165 EELGs (~29%) classified as group members with a probability ≥50% and ≥90% in 46 and 34 of them, respectively. Out of these 48 galaxies, 27 EELGs belong to pairs of galaxies, 11 belong to triplets, and only 10 of them belong to groups of four or more spectroscopic members. The probability that these EELGs are the most massive galaxies of their group is ≤10% for all but five EELGs, all of them in pairs. Only two galaxies in our sample, zCOSMOS ID#823693 and ID#823694, constitute on their own a spectroscopic pair of EELGs. The median properties of EELGs in groups are shown in Table 3.

We find that only ~29% of EELGs are in groups with one or more spectroscopic companions. Thus, we conclude that EELGs

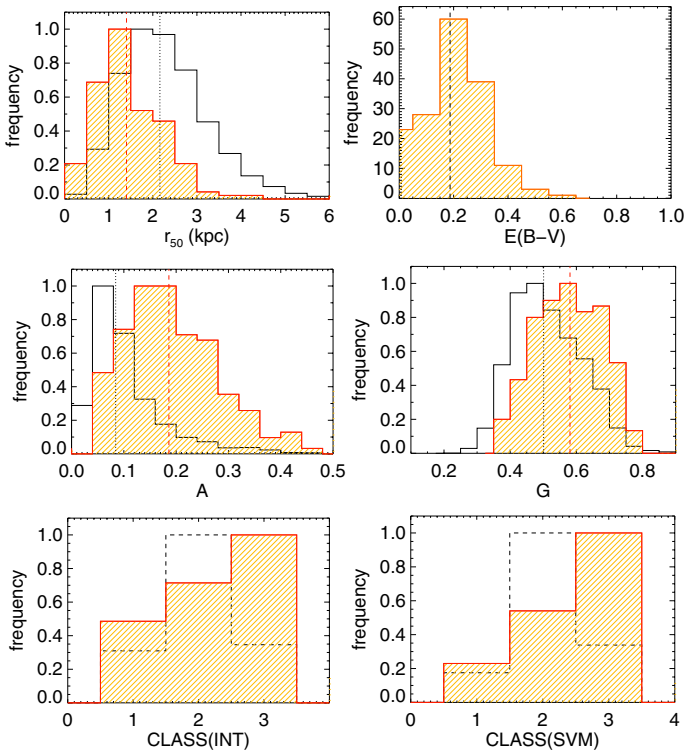


**Fig. 12.** Normalized distribution of morphological parameters and classes for EELG and SFG-20k samples. Panels show, *from the upper left to the bottom right side*, the half-light radius ($r_{50}$), the concentration index (C), the asymmetry (A), and the Gini (G) coefficients, and the morphological classes INT and SVM proposed by Tasca et al. (2009), where 1 = elliptical, 2 = spiral, and 3 = irregular. Lines and colors are as in Fig. 2.

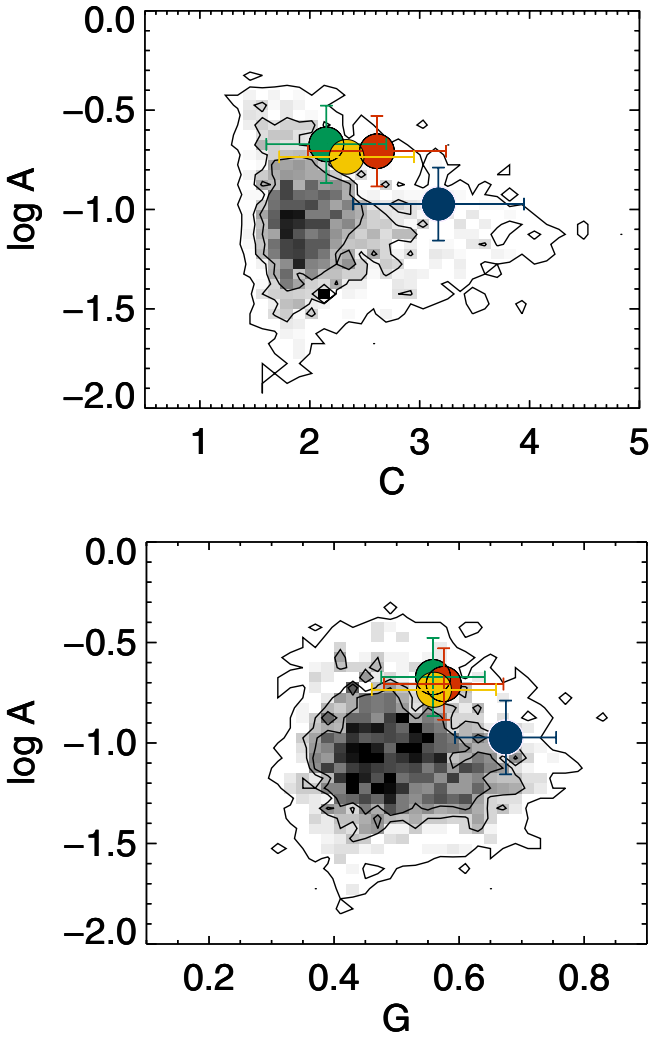


**Fig. 13.** Asymmetry-concentration (*top*) and asymmetry-Gini (*bottom*) diagrams. The gray density plot show the location of the SFG-20k sample. The inner and outer contours enclose 50, 68 and 95% of the sample, respectively. Median values and dispersions for the EELGs are indicated by large color circles and error bars. Yellow, red, green and blue colors indicate EELGs visually classified as "merger/interaction", "cometary/tadpole", "clumpy/chain" and "round/nucleated", respectively.

are located in relative isolation, in agreement with previous findings for local star-forming dwarf galaxies (e.g., Vílchez 1995; Telles & Terlevich 1995; Lee et al. 2000; Noeske et al. 2001; Pustilnik et al. 2001; Koulouridis et al. 2013). It should be noted, however, that the fraction of EELGs members of groups is nearly the same as in the SFR-20k sample. Moreover, most of these groups show a non-negligible number of additional photometric members, which may constitute in most cases neighbors of lower luminosity, so the above numbers should be considered as lower limits. Because of spectroscopic incompleteness we may miss, in these and in the remaining 70% of the EELG sample, possible faint companions that are often seen projected closely to the EELGs.

Faint neighbors can be important, for example, to evaluate the role of interactions in the triggering of star formation. Some observational evidence shows that local star-forming dwarfs are usually found with low-surface-brightness companions (Brosch et al. 2004; Sánchez-Janssen et al. 2013). If these neighbors are located in the very close environment ($\ll$1 Mpc) of the galaxies they may have an influence on the star formation triggering processes and subsequent evolution (Pustilnik et al. 2001). In the case of our EELGs this will be a topic for a future, more detailed investigation.

## 4. Discovery of extremely metal-poor EELGs

Extremely metal-poor (XMP) galaxies are the least evolved systems in the Universe and, therefore, they provide a unique environment in which to study the first stages of galaxy evolution and chemical enrichment (Kunth & Östlin 2000). However, XMPs are extremely scarce (~0.01% of galaxies in the Local Universe; Morales-Luis et al. 2011) and only a handful of bona fide XMPs have been discovered so far at $z > 0.3$ (e.g., Hu et al. 2009; Ly et al. 2014; Maseda et al. 2014; Amorín et al. 2014a).

In the subset of 149 EELGs with reliable metallicities we find six objects (~4%) with metallicities below the limit for XMPs (~1/10 $Z_\odot$, e.g., Kniazev et al. 2004; Ekta & Chengalur 2010). We show two examples in Fig. 14 and summarize their main properties in Table 4. In three EELGs, zCOSMOS ID#836108, ID#701741, and ID#825959, at $z \gtrsim 0.3$ the metallicity has been derived using the electron temperature. However, we are cautious about the metallicity of zCOSMOS ID#836108 because it was derived using the $T$([O III])–$Z$ calibration, which at very low metallicities may underestimate the true metallicity (see Fig. 10). The remaining three EELGs have $z \lesssim 0.3$ and their metallicities have been derived using the $N2$ parameter. One of these, zCOSMOS ID#840952, is the most metal-poor galaxy in our sample ($Z \sim 0.04\ Z_\odot$), and is comparable to the most metal-poor HII galaxies known (e.g., I Zw 18

**Table 4.** The properties of very metal-poor EELGs in zCOSMOS.

| zCOSMOS ID | $z$ | MT | $c(H_\beta)$ | $EW(H\beta)$ | $t_e([O\,III])$ | $\log(O\,III/H\beta)$ | $\log([N\,II]/H\alpha)$ | log(N/O) | 12+log(O/H) |
|---|---|---|---|---|---|---|---|---|---|
| (1) | (2) | (3) | (4) | (5) | (6) | (7) | (8) | (9) | (10) |
| 701741 | 0.504 | 2 | $0.12 \pm 0.05$ | $113 \pm 20$ | $2.28 \pm 0.11$ | $0.50 \pm 0.05$ | ... | ... | $7.46 \pm 0.15^b$ |
| 809215 | 0.124 | 2 | $0.20 \pm 0.07^a$ | ... | ... | ... | $-1.79 \pm 0.18$ | $-1.83 \pm 0.15^e$ | $7.65 \pm 0.07^d$ |
| 825959 | 0.690 | 3 | $0.00 \pm 0.08^a$ | $66 \pm 13$ | $1.87 \pm 0.06$ | $0.52 \pm 0.06$ | ... | ... | $7.56 \pm 0.12^b$ |
| 836108 | 0.351 | 3 | $0.30 \pm 0.13$ | $74 \pm 16$ | $1.92 \pm 0.04$ | $0.77 \pm 0.04$ | ... | ... | $7.47 \pm 0.10^c$ |
| 840051 | 0.250 | 1 | $0.28 \pm 0.04$ | $84 \pm 10$ | ... | $0.61 \pm 0.02$ | $-1.75 \pm 0.11$ | $-2.00 \pm 0.26^e$ | $7.69 \pm 0.08^d$ |
| 840962 | 0.121 | 1 | $0.31 \pm 0.06^a$ | ... | ... | ... | $-2.18 \pm 0.13$ | $-1.75 \pm 0.24^e$ | $7.35 \pm 0.11^d$ |

**Notes.** Columns: (1) zCOSMOS identification number; (2) redshift; (3) morphological type: (1) regular, (2) clumpy/Irregular, (3) cometary/Tadpole; (4) reddening constant from the $H\alpha/H\beta$ ratio, except for those with the superscript $^{(a)}$, which are taken from SED fitting; (5) $H\beta$ equivalent width in Å; (6) [O III] electron temperature in units of $10^4$ K; (7) [O III]5007/$H\beta$ ratio; (8) *N2* parameter; (9) Nitrogen-to-oxygen ratio; (10) gas-phase metallicity; method used to derive metallicity and N/O: $^{(b)}$ = Direct method, $^{(c)}$ = $T([O\,III])$–$Z$, $^{(d)}$ = *N2*, $^{(e)}$ = *N2S2*.

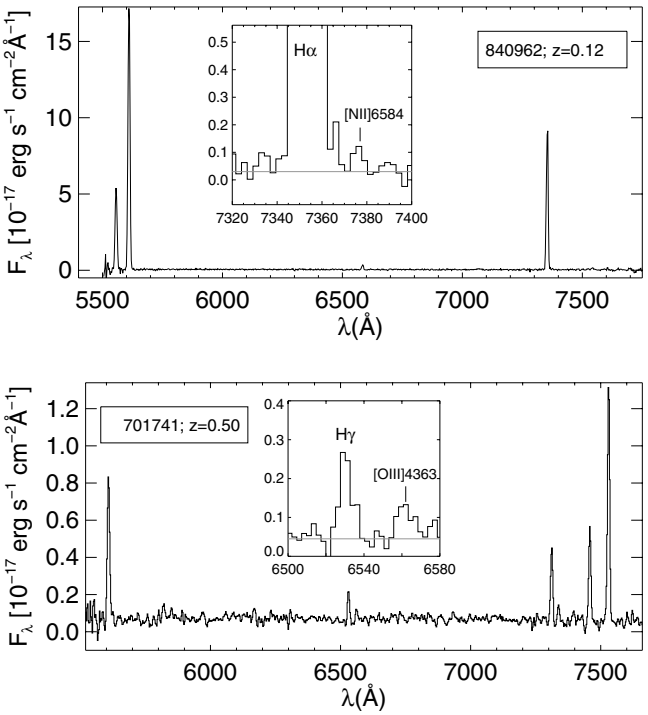


**Fig. 14.** VIMOS spectra of the very metal-poor EELGs zCOSMOS ID#840962 and ID#701741 at $z = 0.12$ and $z = 0.50$, respectively. The spectra have been smoothed by a two-pixel boxcar filter. The insets show a close-up view of the $H\alpha$+[N II] and $H\gamma$+[O III]$\lambda$4363 lines.

and SBS 0335-052; Papaderos et al. 2006; Izotov et al. 2009). Its [N II] line is extremely weak ($S/N \sim 2.5$; Fig. 14), so its flux might be considered as an upper limit. For these three EELGs we have derived the nitrogen-to-oxygen ratio (N/O) using the *N2S2* calibration (Pérez-Montero & Contini 2009). Their very low nitrogen abundance, $\log(N/O) \lesssim -1.7$, is typical of chemically unevolved systems, where the nitrogen is still primarily produced by massive stars (e.g., Mollá et al. 2006). Deeper, high S/N spectroscopy covering the entire spectral range should provide a definitive confirmation of the extremely low oxygen abundance for these EELGs.

An intriguing aspect of XMPs is that over 60% of them turn out to have cometary/tadpole morphologies (Papaderos et al. 2008; Sánchez Almeida et al. 2013; Filho et al. 2013). While cometary/tadpole morphologies are rather common at high redshift (~6–10% of all galaxies in the *Hubble* Ultra Deep Field, Straughn et al. 2006; Elmegreen & Elmegreen 2010), this percentage decreases at lower redshifts (<1% in the local Universe; Elmegreen et al. 2012). Here we find a large number of tadpoles among EELGs and at least half of the most metal-poor EELGs are indeed tadpoles. This can provide additional clues about their nature. Sánchez Almeida et al. (2013) studied their morphological and dynamical properties and suggested that XMPs with tadpole morphologies are in early stages of their disk assembly. In this scenario, a massive accretion of external metal-poor gas feeds the starburst, leading to large inhomogeneities or gradients of metallicity from head to tail (Sánchez Almeida et al. 2014), closely resembling recent findings at higher redshift (e.g., Cresci et al. 2010; Queyrel et al. 2012; Troncoso et al. 2014). Future studies of very metal-poor EELGs using high-quality 3D spectroscopy will be used to test this scenario.

## 5. Lyman-alpha emission in EELGs

High-redshift star-forming galaxies are generally recognized in surveys by their high UV luminosity and/or by their strong Ly$\alpha$ emission, with equivalent widths $EW(Ly\alpha) \geq 20$ (e.g., Shapley et al. 2003; Mallery et al. 2012). Although Ly$\alpha$ selection may systematically trace different galaxies at different redshifts (Nilsson et al. 2011) and a small fraction of Ly$\alpha$ emitters (LAEs) may be evolved galaxies (Pentericci et al. 2009), most of them typically show low metallicity, blue colors, small sizes, and low dust attenuation, indicating an early stage of galaxy formation (e.g., Pirzkal et al. 2007; Cassata et al. 2011; Cowie et al. 2011; Finkelstein et al. 2011). A significant fraction of their low redshift ($z \sim 0.3$) analogues are also found to be EELGs (e.g., Cowie et al. 2011).

Although they were not selected for their UV properties, our sample EELGs are very luminous in the UV continuum, so it is interesting to investigate whether some of these galaxies have been identified as LAEs in the literature. To this end, we cross-correlate our sample with GALEX grism spectroscopy surveys. We find that only four zCOSMOS EELGs at $z = 0.25$–$0.38$ have been observed so far, and they are included in the catalog of low-$z$ GALEX LAEs of Cowie et al. (2010). We identify and show these four EELGs in Fig. 15. Remarkably, all of them show prominent Ly$\alpha$ emission lines, with luminosities

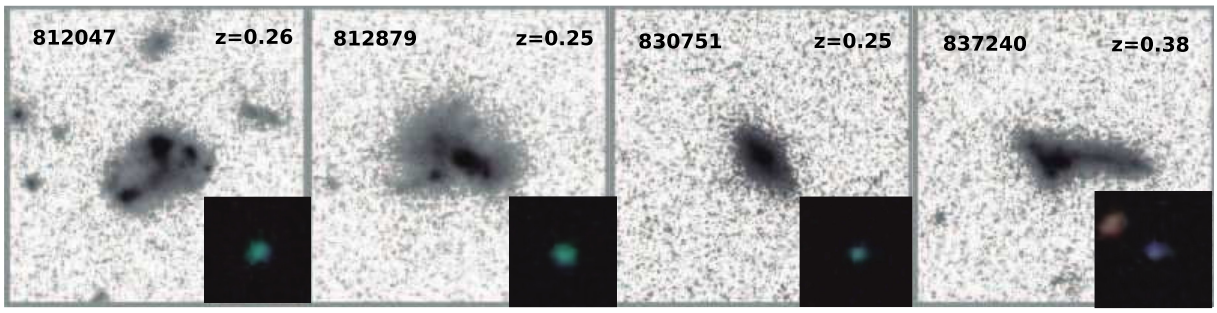


**Fig. 15.** HST/ACS *I*-band images of EELGs with detected Ly$\alpha$ emission. The insets show *ugriz* color-composite SDSS-*DR*9 postage-stamps (*FWHM* ~ 1″) for the same galaxies. Each ACS and SDSS cutouts have 6″ and 30″ on a side, respectively. Labels indicate zCOSMOS ID number and redshift.

$\log(L_{Ly\alpha}) = 41.8–42.4$ erg s$^{-1}$, and high equivalent widths of $EW(Ly\alpha) = 22–45$ Å (rest-frame).

The observed Ly$\alpha$/H$\alpha$ ratios of these EELGs are between 0.5−2, well below the Case B recombination value, even after correction for dust extinction. Comparing their Ly$\alpha$ and H$\alpha$ equivalent widths ($EW(H\alpha) = 320–580$ Å), these galaxies are among those with larger $EW(H\alpha)$ low-$z$ LAEs in the catalog of Cowie et al. (2010). Their $EW(H\alpha)/EW(Ly\alpha)$ ratios (~14) are instead comparable with some high-excitation LAEs at higher redshift (e.g., $z \sim 2$ Finkelstein et al. 2011; Nakajima et al. 2013). Compared with model predictions (e.g., Schaerer 2003), these $EW(H\alpha)/EW(Ly\alpha)$ ratios are in good agreement with tracks for instantaneous burst models with young ages (~$10^7$ yr) and low metallicities (see Nakajima et al. 2013, their Fig. 10), probably superposed with a more constant (e.g., exponentially declining) underlying star formation history (e.g., Amorín et al. 2012a).

As shown in Fig. 15, zCOSMOS EELGs with Ly$\alpha$ emission display a variety of morphologies in HST-ACS imaging, while in SDSS images they appear nearly unresolved. Although considered as green pea galaxies owing to their large $EW$([O III]) and green colors in the SDSS thumbnails, these galaxies were not included in the green pea sample of Cardamone et al. (2009) because of their low luminosity, which is ≳2 mag fainter than the SDSS spectroscopic limits. The connection between LAEs, green peas, and our sample of EELGs is not entirely surprising. Cowie et al. (2011) have shown that ~75% of low-$z$ LAEs have $EW(H\alpha) > 100$ Å, while only ~30% of UV-continuum selected galaxies with $EW(H\alpha) > 100$ Å are LAEs. Moreover, recent studies have found evidence for high-ionization state and low metallicities in LAEs out to $z \gtrsim 2$ (Xia et al. 2012; Nakajima et al. 2013, see also Cassata et al. 2013, for HeII $\lambda$1640 detection in LAEs). These two properties are an imprint of green peas (Amorín et al. 2012a; Jaskot & Oey 2013) and EELGs in general (see Fig. 2). Thus, LAEs could be ubiquitous among low-mass galaxies selected for their unusually large equivalent widths.

## 6. Comparison with other EELG studies

Star-forming galaxies with very high [O III] EWs have been identified at lower and higher redshifts in previous studies, as we mentioned in our introduction. At lower redshift luminous HII galaxies and green peas (Cardamone et al. 2009; Amorín et al. 2010, 2012a) show very similar properties to our EELGs, e.g., very large [O III] EWs up to ~1500 Å, low-metallicity, extreme compactness, and high sSFR. At low to intermediate redshift ($z \lesssim 1$), samples of EELGs selected from narrowband imaging (e.g., Kakazu et al. 2007; Hu et al. 2009) and from very deep spectroscopic surveys for their strong [O III] lines (e.g., Hoyos et al. 2005; Ly et al. 2014; Amorín et al. 2014a) also show strong similarities to our EELG sample. Similar conclusions can be obtained by comparing the properties of zCOSMOS EELGs with EELGs at higher redshift (i.e., $z > 1$), which are typically selected by their unusually strong [O III] EWs in low-resolution HST NIR spectroscopy (e.g., Atek et al. 2011, 2014; van der Wel et al. 2011; Xia et al. 2012; Maseda et al. 2014; Masters et al. 2014). As many of these studies have shown, the overall morphology, size, stellar mass, sSFR, and metallicity properties suggest that EELGs are distributed in the same parameter space.

Scaling relations are useful tools for comparing the observed properties of galaxies and the predictions of models. A thorough analysis of different scaling relations including size, mass, metallicity, and SFR, will be the subject of the second paper of this series. However, we anticipate in Fig. 16 the relation between SFR and stellar mass for the EELGs and SFGs in zCOSMOS, comparing them to other EELGs from the literature. In the SFR-$M_\star$ plane, nearly all EELGs follow a well-defined relation. However, this trend is ~1 dex above the extrapolation to low stellar mass of the main sequence followed by normal SFGs at a given redshift (e.g., Noeske et al. 2007; Elbaz et al. 2007; Whitaker et al. 2012). This means that EELGs have enhanced sSFR at a given stellar mass compared to typical SFGs. Their values, in the range ~$10^{-9}$–$10^{-7}$ yr$^{-1}$, imply short stellar mass doubling times <1 Gyr, which clearly suggest that EELGs are forming stars in strong bursts.

This result is in excellent agreement with similar studies, which have also shown that most EELGs are typically more metal-poor than predicted by the mass-metallicity relation at a given redshift (e.g., Amorín et al. 2014a; Ly et al. 2014). One possible interpretation for the offset position of EELGs in scaling relations involving mass, metallicity, and SFR is that strong gas inflows (e.g., due to interactions or mergers) and outflows (e.g., due to SNe feedback) may play a significant role in regulating their chemical abundances and mass growth (e.g., Amorín et al. 2010; Xia et al. 2012). Finally, another common point among EELGs at low and high redshift is the high-ionization state of their ISM. In our sample we find a common range of high-ionization parameters (as measured by the [O III]/[O II] ratio, see Fig. 10) for EELGs, GPs, and local HII galaxies. Recently Nakajima & Ouchi (2014) show that, for a given stellar mass and SFR, the ionization of GPs and other low-$z$ EELGs is much higher than in typical SDSS SFGs, being only comparable to the ionization found in some high-$z$ LBGs and LAEs.

Overall, in terms of scaling relations involving size, stellar mass, SFR, metallicity, and also the ionization parameter,

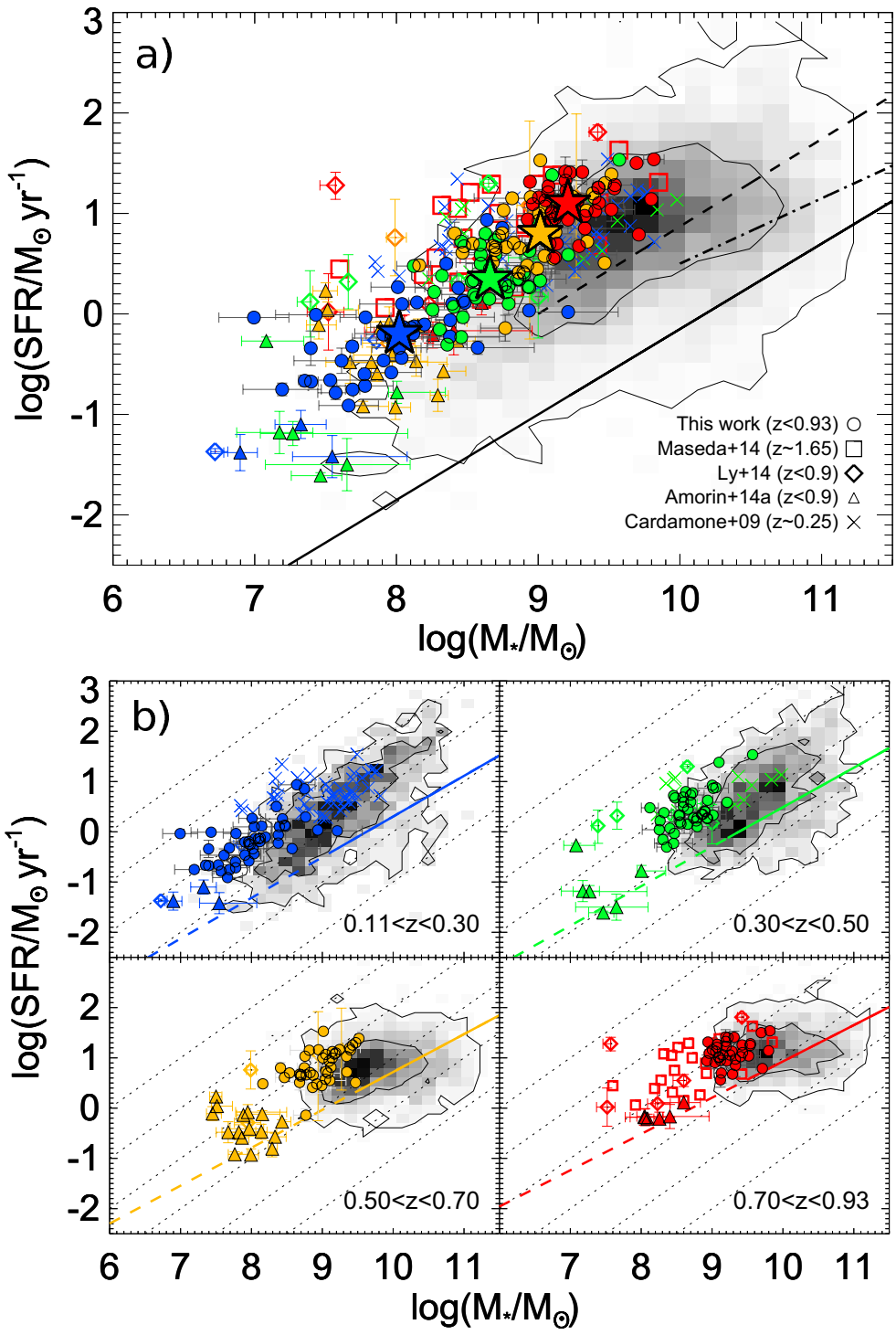


**Fig. 16. a)** Location of EELGs and SFGs in the SFR-$M_*$ plane. The gray density contours show the position of the SFG-20k sample. The inner and outer contours enclose 68% and 99% of the sample, respectively. Big stars show the median values for EELGs (see Table 3). Solid, dot-dashed, and dashed lines show the main sequence (MS) of galaxies at $z = 0$ (Whitaker et al. 2012), $z \sim 0.7$ (Noeske et al. 2007), and $z \sim 1$ (Elbaz et al. 2007), respectively. **b)** Same as **a)** but divided into four redshift bins. Solid and dashed colored lines show the MS of galaxies at each redshift and their extrapolation to the low-mass regime, respectively, according to Whitaker et al. (2012). Dotted lines indicate constant sSFR from $10^{-11}$ yr$^{-1}$ (*bottom left*) to $10^{-6}$ yr$^{-1}$ (*upper right*). At all redshifts the EELGs follow nearly the same relation, which is offset by $\gtrsim$1 dex from the local MS

.

EELGs seem to be a relatively homogeneous class regardless of redshift (e.g., Xia et al. 2012; Ly et al. 2014; Nakajima & Ouchi 2014; Maseda et al. 2014; Amorín et al. 2014a). If true, all these low-mass galaxies are probably being caught in a similar, transient and extreme stage of their formation history, where they are efficiently building up a significant fraction of their present-day stellar mass in a young, galaxy-wide starburst.

Nevertheless, a more detailed and quantitative comparison of the galaxy-averaged EELG properties and number densities through cosmic time is needed to reach firm conclusions on

the physical properties behind the strong star-formation activity at different cosmic epochs. In particular, this comparison should be made using complete samples studied with homogeneous methodologies and high-quality datasets over a wide redshift range. Studies like these, which are currently ongoing, will strongly benefit from the statistical value and wealth of data products provided in this study.

## 7. Summary and conclusions

Using the zCOSMOS 20k bright survey we have selected a large sample of 183 extreme emission-line galaxies (EELGs) at $0.11 \leq z \leq 0.93$ showing unusually high [O III]$\lambda$5007 rest-frame equivalent widths ($EW$([O III]) $\geq$ 100 Å). We have used zCOSMOS optical spectroscopy and multiwavelength COSMOS photometry and HST-ACS $I$-band imaging to characterize the main properties of EELGs, such as sizes, stellar masses, SFR, and metallicity, as well as morphology and large-scale environment. We summarize our main findings as follows:

1. The adopted selection criterion based on EW([O III]) lead to a sample of galaxies with the highest EWs in all the observed strong emission lines, e.g., H$\beta$ ($\gtrsim$20 Å) and H$\alpha$ ($\gtrsim$100 Å), suggesting galaxies dominated by young ($\lesssim$10 Myr) star-forming regions. The EELGs constitute 3.4% of SFGs in our parent zCOSMOS sample. Using emission-line diagnostic diagrams we divided the sample into 165 purely star-forming galaxies plus 18 NL-AGN candidates (∼10%). Only four of them are detected as bright X-ray sources.
2. EELGs form the low-end of stellar mass and the high-end of sSFR distributions of SFGs in zCOSMOS up to $z \sim 1$. Stellar masses of EELGs, as derived from multiband SED fitting, lie in the range $7 \lesssim \log(M_*/M_\odot) \lesssim 10$. Our sample, however, is not complete in mass below $\sim 10^9\,M_\odot$ in the considered redshift range. Star formation rates from both H$\alpha$ and FUV luminosities after corrections for dust attenuation and extinction are consistent with each other and range $0.1 \lesssim SFR \lesssim 35\,M_\odot\,\mathrm{yr}^{-1}$ (Chabrier IMF). Both quantities increase similarly with redshift, so this results in a tight range of specific SFRs (median $\mathrm{s}SFR = 10^{-8.18}\,\mathrm{yr}^{-1}$) and stellar mass doubling times $0.01\,\mathrm{Gyr} < M_*/SFR < 1\,\mathrm{Gyr}$.
3. EELGs are characterized by their low metallicities, $7.3 \lesssim 12+\log(\mathrm{O/H}) \lesssim 8.5$ ($0.05-0.6\,Z_\odot$), as derived using both the direct measurements based on electron temperature ($t_e$) and strong-line methods calibrated consistently with galaxies with $t_e$ measurements. Therefore, the chemical abundances of EELGs at $0.11 \leq z \leq 0.93$ are very similar to those of nearby HII galaxies and BCDs. We find six (∼4%) extremely metal-poor ($Z < 0.1\,Z_\odot$) galaxies in our sample.
4. EELGs are moderately low-dust, very compact $UV$-luminous galaxies, as evidenced by their typically blue colors ($\beta \sim -1.6$), high $FUV$ luminosities ($L_{\mathrm{FUV}} \sim 10^{10.4}\,L_\odot$) and high surface brightnesses $\mu_{\mathrm{FUV}} \gtrsim 10^9\,L_\odot\,\mathrm{kpc}^{-2}$. We find only four EELGs with GALEX-UV spectroscopic observations. All these galaxies are strong Ly$\alpha$ emitters, with large equivalent widths and luminosities in the ranges $EW(\mathrm{Ly}\alpha)$ = 22–45 Å and $\log(L_{\mathrm{Ly}\alpha}) = 41.8-42.4\,\mathrm{erg\,s}^{-1}$, respectively.
5. Using HST-ACS $I$-band COSMOS images we classify star-forming EELGs into four morphological classes according to the distribution and shape of their high- and low-surface-brightness components (i.e., SF knots and underlying galaxy, respectively). We show that 18% have round/nucleated morphologies, most of which are barely resolved, while the remaining 82% have irregular morphologies. These irregular morphologies are visually classified as clumpy/chain (37%), cometary/tadpole (16%), and merger/interacting (29%). Therefore, we conclude that at least ∼80% of the EELG sample shows non-axisymmetric morphologies. Using quantitative morphological parameters we find that EELGs show smaller half-light radii ($r_{50} \sim 1.3$ kpc in the median) and larger concentration, asymmetry, and Gini parameters than other SFGs in zCOSMOS, most of them being classified as irregular galaxies by automated algorithms. Among the defined morphological classes we do not find any significant difference in the redshift distribution or physical properties.
6. As star-forming dwarfs in the Local Universe, EELGs are usually found in relative isolation. While only very few EELGs belong to compact groups, almost one third of them are found in spectroscopically confirmed loose pairs or triplets. Comparing isolated and grouped EELGs we do not find any significant differences in the redshift distributions or physical properties.

In conclusion, we have shown that galaxies selected by their extreme strength of optical emission lines led us to a homogeneous, representative sample of compact, low-mass, low-metallicity, vigorously star-forming systems identifiable with luminous, higher-$z$ versions of nearby HII galaxies and blue compact dwarfs. The extreme properties of some of these rare systems closely resemble those of luminous compact galaxies, such as the green peas (Cardamone et al. 2009; Amorín et al. 2010) and other samples of emission line galaxies with very high equivalent widths recently found at similar and higher redshift (e.g., Hoyos et al. 2005; Kakazu et al. 2007; Salzer et al. 2009; Izotov et al. 2011; Atek et al. 2011; van der Wel et al. 2011, 2013; Xia et al. 2012; Shim & Chary 2013; Henry et al. 2013; Ly et al. 2014; Maseda et al. 2014; Amorín et al. 2014b). The EELGs are galaxies likely caught in a transient and early period of their evolution, where they are efficiently building up a significant fraction of their present-day stellar mass in a young, galaxy-wide starburst. Therefore, they constitute an ideal benchmark for comparative studies with samples of high redshift Ly$\alpha$ emitters and Lyman-break galaxies of similar mass and high-ionization state.

*Acknowledgements.* We thank the referee for her/his deep and thorough reports which significantly contributed to improving this manuscript. We also gratefully acknowledge Polychronis Papaderos, Marco Castellano, Veronica Sommariva, Jorge Sánchez Almeida and Casiana Muñoz-Tuñón for a careful reading of the paper and the helpful comments and suggestions provided. We also thank M. Maseda and A. van der Wel for kindly providing us assistance with their data. This work was partially funded by the Spanish MICINN under the Consolider-Ingenio 2010 Program grant CSD2006-00070: First Science with the GTC[9], and by projects AYA2007-67965-C03-02 and AYA2010-21887-C04-01 of the Spanish National Plan for Astronomy and Astrophysics, and by the project TIC114 *Galaxias y Cosmología* of the Junta de Andalucía (Spain). R.A. acknowledges the contribution of the FP7 SPACE project ASTRODEEP (Ref. No: 312725), supported by the European Commission. This work has also been partially supported by the CNRS-INSU and its Programmes Nationaux de Galaxies et de Cosmologie (France). The VLT-VIMOS observations have been carried out on guaranteed time (GTO) allocated by the European Southern Observatory (ESO) to the VIRMOS consortium, under a contractual agreement between the Centre National de la Recherche Scientifique of France, heading a consortium of French and Italian institutes, and ESO, to design, manufacture and test the VIMOS instrument. Based on observations obtained with MegaPrime/MegaCam, a joint project of CFHT and CEA/DAPNIA, at the Canada-France-Hawaii Telescope (CFHT) which is operated by the National Research Council (NRC) of Canada, the Institut National des Science de l'Univers of the Centre National de la Recherche Scientifique (CNRS) of France

[9] http://www.iac.es/consolider-ingenio-gtc

and the University of Hawaii. This work is based in part on data products produced at TERAPIX and the Canadian Astronomy Data Centre as part of the Canada-France-Hawaii Telescope Legacy Survey, a collaboration project of NRC and CNRS.

## References


Abazajian, K., Adelman-McCarthy, J. K., Agüeros, M. A., et al. 2003, AJ, 126, 2081
Abraham, R. G., van den Bergh, S., Glazebrook, K., et al. 1996, ApJS, 107, 1
Allende Prieto, C., Lambert, D. L., & Asplund, M. 2001, ApJ, 556, L63
Amorín, R., Alfonso, J., Aguerri, J. A. L., Muñoz-Tuñón, C., & Cairós, L. M. 2009, A&A, 501, 75
Amorín, R. O., Pérez-Montero, E., & Vílchez, J. M. 2010, ApJ, 715, L128
Amorín, R., Pérez-Montero, E., Vílchez, J. M., & Papaderos, P. 2012a, ApJ, 749, 185
Amorín, R., Vílchez, J. M., Hägele, G. F., et al. 2012b, ApJ, 754, L22
Amorín, R., Grazian, A., Castellano, M., et al. 2014a, ApJ, 788, L4
Amorín, R., Sommariva, V., Castellano, M., et al. 2014b, A&A, 568, L8
Atek, H., Siana, B., Scarlata, C., et al. 2011, ApJ, 743, 121
Atek, H., Kneib, J.-P., Pacifici, C., et al. 2014, ApJ, 789, 96
Baldwin, J. A., Phillips, M. M., & Terlevich, R. 1981, PASP, 93, 5
Bertoldi, F., Carilli, C., Aravena, M., et al. 2007, ApJS, 172, 132
Bolzonella, M., Kovač, K., Pozzetti, L., et al. 2010, A&A, 524, A76
Brosch, N., Almoznino, E., & Heller, A. B. 2004, MNRAS, 349, 357
Bruzual, G. & Charlot, S. 2003, MNRAS, 344, 1000
Cairós, L. M., Caon, N., Vílchez, J. M., González-Pérez, J. N., & Muñoz-Tuñón, C. 2001, ApJS, 136, 393
Capak, P., Aussel, H., Ajiki, M., et al. 2007, ApJS, 172, 99
Cardamone, C., Schawinski, K., Sarzi, M., et al. 2009, MNRAS, 399, 1191
Cardelli, J. A., Clayton, G. C., & Mathis, J. S. 1989, ApJ, 345, 245
Calzetti, D., Armus, L., Bohlin, R. C., et al. 2000, ApJ, 533, 682
Cassata, P., Le Fèvre, O., Garilli, B., et al. 2011, A&A, 525, A143
Cassata, P., Le Fevre, O., Charlot, S., et al. 2013, A&A, 556, A68
Castellano, M., Sommariva, V., Fontana, A., et al. 2014, A&A, 566, A19
Chabrier, G. 2003, PASP, 115, 763
Charlot, S., & Longhetti, M. 2001, MNRAS, 323, 887
Chen, T.-W., Smartt, S. J., Bresolin, F., et al. 2013, ApJ, 763, L28
Christensen, L., Hjorth, J., & Gorosabel, J. 2004, A&A, 425, 913
Conselice, C. J. 2003, ApJS, 147, 1
Cowie, L. L., Barger, A. J., & Hu, E. M. 2010, ApJ, 711, 928
Cowie, L. L., Barger, A. J., & Hu, E. M. 2011, ApJ, 738, 136
Cresci, G., Mannucci, F., Maiolino, R., et al. 2010, Nature, 467, 811
Curtis-Lake, E., McLure, R. J., Dunlop, J. S., et al. 2013, MNRAS, 429, 302
Denicoló, G., Terlevich, R., & Terlevich, E. 2002, MNRAS, 330, 69
Ekta, B., & Chengalur, J. N. 2010, MNRAS, 406, 1238
Elbaz, D., Daddi, E., Le Borgne, D., et al. 2007, A&A, 468, 33
Elmegreen, B. G., & Elmegreen, D. M. 2010, ApJ, 722, 1895
Elmegreen, D. M., Elmegreen, B. G., Sánchez Almeida, J., et al. 2012, ApJ, 750, 95
Elmegreen, B. G., Elmegreen, D. M., Sánchez Almeida, J., et al. 2013, ApJ, 774, 86
Elvis, M., Civano, F., Vignali, C., et al. 2009, ApJS, 184, 158
Filho, M. E., Winkel, B., Sánchez Almeida, J., et al. 2013, A&A, 558, A18
Finkelstein, S. L., Hill, G. J., Gebhardt, K., et al. 2011, ApJ, 729, 140
Guaita, L., Francke, H., Gawiser, E., et al. 2013, A&A, 551, A93
Guseva, N. G., Izotov, Y. I., Fricke, K. J., & Henkel, C. 2011, A&A, 534, A84
Guzman, R., Gallego, J., Koo, D. C., et al. 1997, ApJ, 489, 559
Hägele, G. F., Díaz, Á. I., Terlevich, E., et al. 2008, MNRAS, 383, 209
Hasinger, G., Cappelluti, N., Brunner, H., et al. 2007, ApJS, 172, 29
Henry, A., Martin, C. L., Finlator, K., & Dressler, A. 2013, ApJ, 769, 148
Hoyos, C., Koo, D. C., Phillips, A. C., Willmer, C. N. A., & Guhathakurta, P. 2005, ApJ, 635, L21
Hu, E. M., Cowie, L. L., Kakazu, Y., & Barger, A. J. 2009, ApJ, 698, 2014
Huertas-Company, M., Rouan, D., Tasca, L., Soucail, G., & Le Fèvre, O. 2008, A&A, 478, 971
Izotov, Y. I., Guseva, N. G., Fricke, K. J., & Papaderos, P. 2009, A&A, 503, 61
Izotov, Y. I., Guseva, N. G., & Thuan, T. X. 2011, ApJ, 728, 161
Jaskot, A. E., & Oey, M. S. 2013, ApJ, 766, 91
Juneau, S., Dickinson, M., Alexander, D. M., & Salim, S. 2011, ApJ, 736, 104
Kakazu, Y., Cowie, L. L., & Hu, E. M. 2007, ApJ, 668, 853
Kauffmann, G., Heckman, T. M., Tremonti, C., et al. 2003, MNRAS, 346, 1055
Kennicutt, R. C., Jr. 1998, ApJ, 498, 541
Kennicutt, R. C., & Evans, N. J. 2012, ARA&A, 50, 531
Kewley, L. J., & Ellison, S. L. 2008, ApJ, 681, 1183
Kewley, L. J., Dopita, M. A., Sutherland, R. S., Heisler, C. A., & Trevena, J. 2001, ApJ, 556, 121
Kewley, L. J., Brown, W. R., Geller, M. J., Kenyon, S. J., & Kurtz, M. J. 2007, AJ, 133, 882
Kniazev, A. Y., Pustilnik, S. A., Grebel, E. K., Lee, H., & Pramskij, A. G. 2004, ApJS, 153, 429
Knobel, C., Lilly, S. J., Iovino, A., et al. 2009, ApJ, 697, 1842
Knobel, C., Lilly, S. J., Iovino, A., et al. 2012, ApJ, 753, 121
Kobulnicky, H. A., Willmer, C. N. A., Phillips, A. C., et al. 2003, ApJ, 599, 1006
Koekemoer, A. M., Aussel, H., Calzetti, D., et al. 2007, ApJS, 172, 196
Koo, D. C., Guzman, R., Faber, S. M., et al. 1995, ApJ, 440, L49
Koulouridis, E., Plionis, M., Chávez, R., et al. 2013, A&A, 554, A13
Krueger, H., Fritze-v. Alvensleben, U., & Loose, H.-H. 1995, A&A, 303, 41
Kunth, D., & Östlin, G. 2000, A&ARv, 10, 1
Lamareille, F. 2007, Ph.D. Thesis
Lamareille, F., Mouhcine, M., Contini, T., Lewis, I., & Maddox, S. 2004, MNRAS, 350, 396
Lamareille, F., Contini, T., Le Borgne, J.-F., et al. 2006a, A&A, 448, 893
Lamareille, F., Contini, T., Brinchmann, J., et al. 2006b, A&A, 448, 907
Lamareille, F., Brinchmann, J., Contini, T., et al. 2009, A&A, 495, 53
Lee, J. C., Salzer, J. J., Law, D. A., & Rosenberg, J. L. 2000, ApJ, 536, 606
Leitherer, C., Schaerer, D., Goldader, J. D., et al. 1999, ApJS, 123, 3
Leloudas, G., Schulze, S., Krühler, T., et al. 2015, MNRAS, 449, 917
Le Fèvre, O., Saisse, M., Mancini, D., et al. 2003, Proc. SPIE, 4841, 1670
Lilly, S. J., Le Fèvre, O., Renzini, A., et al. 2007, ApJS, 172, 70
Lilly, S. J., Le Brun, V., Maier, C., et al. 2009, ApJS, 184, 218
López-Sánchez, Á. R., Dopita, M. A., Kewley, L. J., et al. 2012, MNRAS, 426, 2630
Lotz, J. M., Primack, J., & Madau, P. 2004, AJ, 128, 163
Lunnan, R., Chornock, R., Berger, E., et al. 2013, ApJ, 771, 97
Ly, C., Malkan, M. A., Nagao, T., et al. 2014, ApJ, 780, 122
Mallery, R. P., Mobasher, B., Capak, P., et al. 2012, ApJ, 760, 128
Maraston, C. 2005, MNRAS, 362, 799
Marocco, J., Hache, E., & Lamareille, F. 2011, A&A, 531, A71
Martin, D. C., Fanson, J., Schiminovich, D., et al. 2005, ApJ, 619, L1
Maseda, M. V., van der Wel, A., da Cunha, E., et al. 2013, ApJ, 778, L22
Maseda, M. V., van der Wel, A., Rix, H.-W., et al. 2014, ApJ, 791, 17
Masegosa, J., Moles, M., & Campos-Aguilar, A. 1994, ApJ, 420, 576
Masters, D., McCarthy, P., Siana, B., et al. 2014, ApJ, 785, 153
McCracken, H. J., Capak, P., Salvato, M., et al. 2010, ApJ, 708, 202
McGaugh, S. S. 1991, ApJ, 380, 140
Meurer, G. R., Heckman, T. M., & Calzetti, D. 1999, ApJ, 521, 64
Mollá, M., Vílchez, J. M., Gavilán, M., & Díaz, A. I. 2006, MNRAS, 372, 1069
Morales-Luis, A. B., Sánchez Almeida, J., Aguerri, J. A. L., & Muñoz-Tuñón, C. 2011, ApJ, 743, 77
Nakajima, K., & Ouchi, M. 2014, MNRAS, 442, 900
Nakajima, K., Ouchi, M., Shimasaku, K., et al. 2013, ApJ, 769, 3
Nilsson, K. K., Östlin, G., Møller, P., et al. 2011, A&A, 529, A9
Noeske, K. G., Iglesias-Páramo, J., Vílchez, J. M., Papaderos, P., & Fricke, K. J. 2001, A&A, 371, 806
Noeske, K. G., Weiner, B. J., Faber, S. M., et al. 2007, ApJ, 660, L43
Overzier, R. A., Heckman, T. M., Kauffmann, G., et al. 2008, ApJ, 677, 37
Pacifici, C., da Cunha, E., Charlot, S., et al. 2015, MNRAS, 447, 786
Pagel, B. E. J., Edmunds, M. G., Blackwell, D. E., Chun, M. S., & Smith, G. 1979, MNRAS, 189, 95
Papaderos, P., Izotov, Y. I., Fricke, K. J., Thuan, T. X., & Guseva, N. G. 1998, A&A, 338, 43
Papaderos, P., Guseva, N. G., Izotov, Y. I., et al. 2006, A&A, 457, 45
Papaderos, P., Guseva, N. G., Izotov, Y. I., & Fricke, K. J. 2008, A&A, 491, 113
Pentericci, L., Grazian, A., Fontana, A., et al. 2009, A&A, 494, 553
Pérez-Montero, E. 2014, MNRAS, 441, 2663
Pérez-Montero, E., & Contini, T. 2009, MNRAS, 398, 949
Pérez-Montero, E., & Díaz, A. I. 2003, MNRAS, 346, 105
Pérez-Montero, E., & Díaz, A. I. 2005, MNRAS, 361, 1063
Pérez-Montero, E., Contini, T., Lamareille, F., et al. 2013, A&A, 549, A25
Pettini, M., Shapley, A. E., Steidel, C. C., et al. 2001, ApJ, 554, 981
Phillips, A. C., Guzman, R., Gallego, J., et al. 1997, ApJ, 489, 543
Pirzkal, N., Malhotra, S., Rhoads, J. E., & Xu, C. 2007, ApJ, 667, 49
Pustilnik, S. A., Kniazev, A. Y., Lipovetsky, V. A., & Ugryumov, A. V. 2001, A&A, 373, 24
Queyrel, J., Contini, T., Kissler-Patig, M., et al. 2012, A&A, 539, A93
Rosa-González, D., Schmitt, H. R., Terlevich, E., & Terlevich, R. 2007, ApJ, 654, 226
Salzer, J. J., Williams, A. L., & Gronwall, C. 2009, ApJ, 695, L67
Sánchez Almeida, J., Terlevich, R., Terlevich, E., Cid Fernandes, R., & Morales-Luis, A. B. 2012, ApJ, 756, 163
Sánchez Almeida, J., Muñoz-Tuñón, C., Elmegreen, D. M., Elmegreen, B. G., & Méndez-Abreu, J. 2013, ApJ, 767, 74

Sánchez Almeida, J., Morales-Luis, A. B., Muñoz-Tuñón, C., et al. 2014, ApJ, 783, 45
Sánchez-Janssen, R., Amorín, R., García-Vargas, M., et al. 2013, A&A, 554, A20
Sanders, D. B., Salvato, M., Aussel, H., et al. 2007, ApJS, 172, 86
Santini, P., Ferguson, H. C., Fontana, A., et al. 2015, ApJ, 801, 97
Sargent, W. L. W., & Searle, L. 1970, ApJ, 162, L155
Savaglio, S., Glazebrook, K., & Le Borgne, D. 2009, ApJ, 691, 182
Searle, L., & Sargent, W. L. W. 1972, ApJ, 173, 25
Scoville, N., Aussel, H., Brusa, M., et al. 2007, ApJS, 172, 1
Schaerer, D. 2003, A&A, 397, 527
Schaerer, D., & de Barros, S. 2009, A&A, 502, 423
Shapley, A. E., Steidel, C. C., Pettini, M., & Adelberger, K. L. 2003, ApJ, 588, 65
Schiminovich, D., Wyder, T. K., Martin, D. C., et al. 2007, ApJS, 173, 315
Schinnerer, E., Smolčić, V., Carilli, C. L., et al. 2007, ApJS, 172, 46
Shim, H., & Chary, R.-R. 2013, ApJ, 765, 26
Stark, D. P., Schenker, M. A., Ellis, R., et al. 2013, ApJ, 763, 129
Storchi-Bergmann, T., Calzetti, D., & Kinney, A. L. 1994, ApJ, 429, 572
Storey, P. J., & Hummer, D. G. 1995, MNRAS, 272, 41
Straughn, A. N., Cohen, S. H., Ryan, R. E., et al. 2006, ApJ, 639, 724
Taniguchi, Y., Scoville, N., Murayama, T., et al. 2007, ApJS, 172, 9
Tasca, L. A. M., Kneib, J.-P., Iovino, A., et al. 2009, A&A, 503, 379
Telles, E., & Terlevich, R. 1995, MNRAS, 275, 1
Terlevich, R., Melnick, J., Masegosa, J., Moles, M., & Copetti, M. V. F. 1991, A&AS, 91, 285
Thöne, C. C., de Ugarte Postigo, A., García-Benito, R., et al. 2014, MNRAS, submitted [arXiv:1411.1104]
Thuan, T. X., & Martin, G. E. 1981, ApJ, 247, 823
Tremonti, C. A., Heckman, T. M., Kauffmann, G., et al. 2004, ApJ, 613, 898
Troncoso, P., Maiolino, R., Sommariva, V., et al. 2014, A&A, 563, A58
Trump, J. R., Weiner, B. J., Scarlata, C., et al. 2011, ApJ, 743, 144
van der Wel, A., Straughn, A. N., Rix, H.-W., et al. 2011, ApJ, 742, 111
van der Wel, A., van de Ven, G., Maseda, M., et al. 2013, ApJ, 777, L17
Veilleux, S., & Osterbrock, D. E. 1987, ApJS, 63, 295
Vílchez, J. M. 1995, AJ, 110, 1090
Whitaker, K. E., van Dokkum, P. G., Brammer, G., & Franx, M. 2012, ApJ, 754, L29
Xia, L., Malhotra, S., Rhoads, J., et al. 2012, AJ, 144, 28
Yan, R., Ho, L. C., Newman, J. A., et al. 2011, ApJ, 728, 38
Zamojski, M. A., Schiminovich, D., Rich, R. M., et al. 2007, ApJS, 172, 468